Development of a Reconstruction Method for Major Vortex Structure around Tandem Flapping Wing Object via Vortex Trajectory Method

Naohiko Ban[1] , Wataru Yamazaki[2],
Department of Energy and Environment Science, Nagaoka University of Technology, Niigata, 940-2188, Japan

and

Vitaliy Kurlin[3]
Department of Computer Science, University of Liverpool, Liverpool L69 3BX, United Kingdom

Flapping wing micro air vehicle (MAV) is expected to apply in unmanned operations under risky / ultimate conditions. The MAV has to fly in low Reynolds number conditions. Previous researches indicated that flights by flapping motions as insects had higher performance at low Reynolds numbers. In nature, some insects have four flapping wings and achieve excellent flight performance such as hovering and steep turn. This is considered to be the effect of aerodynamic interference between fore and aft wings. The fluid mechanics of the flapping wing are, however, more difficult than traditional fixed wing due to its complex unsteady fluid physics at low Reynolds numbers. Therefore, there are various flight mechanisms within the flapping wing flight and these have not yet been fully clarified. Particle Image Velocimetry (PIV) is an efficient flow measurement technique which can measure such complex flowfield at one time. The visualization of the vorticity distribution is important for understanding the flowfield of the flapping wing object. On the other hand, however, the vorticity distribution obtained through image processing such as PIV analysis is difficult to understand the detailed vortex flowfield due to the data error or noisiness in the flowfield. In this research, therefore, we developed a reconstruction method of vorticity distribution as postprocessing method of PIV measurement for the purpose to assist the physical understanding of the noisy vorticity distribution. The developed method could clearly reconstruct small vortex structures in the backward of the flapping wing object which was difficult to discriminate by conventional vorticity visualizations.

I. Introduction

Inspection of disaster situation and collection of disaster information are important for the optimal action under risky / ultimate conditions such as earthquake or tsunami hazard. In conventional method, manned helicopters have used for the inspection and collection of that. However, the pilots of the helicopters have a risk of secondary disasters depending on the disaster situation. Besides, it is impossible to collect the disaster information in the affected area designated as danger zones. Therefore, the research and development of unmanned aircraft for reducing and preventing the risk has attracted a lot of attention [1-5].

In unmanned aircraft, there are some different flight forms such as fixed wing object, rotary wing object and flapping wing object. Since exploring narrow spots such as collapsed building to explore missing persons is required in the disaster situations, the unmanned objects needs to be miniaturized. However, it has been reported that the miniaturized fixed wing objects or miniaturized rotary wing objects will be in unstable flight [1]. With respect to this problem, from the viewpoint of biomimetics, we focus on birds and insects that are flying creatures in nature. Birds and insects have excellent flight performance such as hovering (stopping in the air) and sudden turning even with those miniaturized sizes. It is considered to be possible to get disaster information safely by developing a miniaturized

[1] Ph. D. Student, Department of Energy and Environment Science, Nagaoka University of Technology
[2] Associate Professor, Department of Mechanical Engineering, Nagaoka University of Technology, Member AIAA
[3] Associate Professor, Department of Computer Science, University of Liverpool

flapping wing object mimicking insects. In fluid dynamics studies on flapping wings, there are simulation-based methods such as “Computational Fluid Dynamics" [3-4] and experimental-based methods such as "Particle Image Velocimetry Analysis" [6-7]. In the simulation-based method, there is a motion optimization of the flapping wing object using the Adjoint method [3]. However, since the flowfield around the flapping wing object is very complicated unsteady flow, the flight mechanism and the fluid physics have not been fully elucidated. In addition, from the viewpoint of the computational cost of the unsteady numerical fluid analysis for complicated wing shape and the lack of knowledge for verifying the analysis accuracy, in this research, we conducted the experiment-based method. In the experiment-based method, Particle Image Velocimetry (PIV) is widely used as a measurement method of the flow velocity distribution at once [8]. In the PIV process, discriminable particle markers called tracer particles are mixed in the flow, and then high-speed shooting is performed with a high-speed camera. The displacements of the tracer particles are estimated by the PIV analysis. Since PIV is a measurement method which does not require any contact type probes such as a Pitot tube or a hot wire current meter, it is possible to measure flowfield with a minimum influence on the flowfield.

In our previous researches, PIV and thrust force measurement for a single (two wing surfaces) flapping wing object as well as a tandem (four wing surfaces) flapping wing object have been carried out [8,9]. The results showed that the thrust force was changed by the flapping phase difference β, wing spacing between the fore and aft wings w, and feathering angle φ. The results of flow visualization and thrust force measurement of the single / tandem flapping wing objects contributed to understand its flow physics. The thrust forces in many tandem cases were more than twice of that of the single flapping wing which indicated the superiority of the tandem flapping wing configuration. With respect to the effects of the flapping phase difference β and the wing spacing w, the highest mean induced velocity was observed at the case of w=25 [mm], β=270 [deg]. This result was obtained by the reason that the induced flow generated from the fore wing was accelerated by the Leading Edge Vortex (LEV) of the aft wing. Except the cases of β=0 [deg], larger wing spacings provided higher mean induced velocities. With respect to the effects of the flapping phase difference β and the feathering angle φ, the highest mean thrust force was obtained at the case of $\varphi=\pm 40$ [deg], β=90 [deg]. At the case of φ=-20~+40 [deg], β=0 [deg], the phenomenon called wake capture was observed in which the energy of induced (wake) flow is recovered and more fluid force can be obtained at the moment changing from downstroke to upstroke motion.

The previous studies show that the vortex structure is important for the flight of the flapping wing object. However, it is difficult to understand the detailed flowfield from vorticity magnitude which is generally used to extract dominant vortices. There are several problems in physical understanding of the vortex structure such as necessity to set the vorticity threshold manually in order to extract dominant vortices, impossibility to visualize small vortices below the threshold, and impossibility to trace the vortex trajectory. In order to solve these problems, we try to extract vortex structures not by using theoretical methods such as Q-creterion but by using machine learning and/or computer vision techniques. In this research, we develop a reconstruction method for major vortex structures around the tandem flapping wing object via a vortex trajectory method which can facilitate the physical understanding of complex vortical flowfield.

II. Experimental Approach

In this section, the experimental set up for the flapping wing object is introduced.

A. Experimental equipment

Outline of the experimental set up is summarized in Fig. 1. A high-speed camera takes sequential images in the enclosed region on the size of 2.4 [m] length × 2.4 [m] width × 1.9 [m] height as shown in Fig. 1.a. In the enclosed region, the tandem flapping wing object is installed at the end of the cantilever and smoke is injected into the enclosed region as tracer particles. Then, the flowfield can be observed by irradiating laser light sheet at the measurement cross sectional position. DPGL-2W 1 [mm] thick Nd: YAG laser manufactured by Japan laser Inc. was used for the light source. The measurement cross section position is set to the 60% semi-span position which passes both top and bottom points of the wing-tip of flapping wing. GX-8 manufactured by nac Image Technology Inc. was used as the high-speed camera and sequential images of 1024×1280 [pixels] was taken at a shooting speed of 1000 [fps] and a shooting period for 13 flapping cycles (about 3 [s] and 3000 images). Oil mist is used for the tracer particles and is vaporized to convert into smoke. Then, the smoke is scattered into the enclosed region. The traceability of particles is an important factor for tracer particles. The traceability of the particles is evaluated by the particle time constant τ_P which represents the time when stationary particles are accelerated to 63% of the fluid velocity. In general, τ_P of 10^{-3} is required for sufficient traceability. The particle time constant is expressed by the following equation [10].

$$\tau_P = \frac{2\rho_P + \rho_F}{36\mu} d^2 \quad (2.\ 1)$$

Here, ρ_F is the fluid density = 0.001247 [g/cm^3], ρ_P is the particle density = 1.0 [g/cm^3], μ is the fluid viscosity = 0.0001712 [g/ms], and d is the particle diameter. From this equation, it can be understand that if the particle size is about 17 [μm] or less, the particle has sufficient traceability. Since the diameter of the tracer particles is almost 4 [μm] or less in the present experimental apparatus, it is considered that there is no problem in the traceability of the particles.

B. Specifications of the tandem flapping wing object

The tandem flapping wing object is shown in Fig. 1.b. The overall wing width of the tandem flapping wing object is 306 [mm], the chord length is 30 [mm], and the fore / aft wings are arranged at intervals of 25 [mm]. A carbon rod is used for the front edge frame of all wings. The rigid wing is expressed by using cardboard as the wing film. On the surface of the wing, black antireflective coating is applied to prevent from reflection by laser light source as much as possible. MK07-17 is used for the DC motor. The motor cover and other supporting parts are made using AR-M1 resin with AGILISTA-3100 3D-printer manufactured by KEYENCE CORPORATION. The weight of the wing is 3.3 [g] per sheet. The total weight of the tandem flapping wing object including the balsa material between the front/rear parts, 3D-printer resin, the carbon rod, and the motor is about 36 [g].

Schematic diagrams of the phase difference control mechanism and the feathering angle control mechanism of the tandem flapping wing object are shown in Fig. 1.c and Fig. 1.d. This object operates with a DC motor located close to the center of the fore-wing mounting parts as power. The lowermost gear is rotated by the link mechanism of the gear from the rotational motion of the DC motor. Flapping motion is performed by converting the lowermost rotational motion into the simple harmonic motion. Here, it is possible to adjust the flapping angle by changing the length of the conversion shaft (Fig. 1.c red lines). The amplitude of the flapping angle α is fixed to ± 45 [deg] for both of the fore / aft wings. With respect to the flapping phase θ of the wing, the top dead center of the fore wing is defined as 0 [deg] of the flapping phase and the bottom dead center of the fore wing is defined as 180 [deg] of the flapping phase. In addition, the lowermost rotational motion also rotates the gear on the aft wing side through the carbon shaft. There is a same mechanism to make the simple harmonic motion at the aft wing which makes it possible to flap both fore and aft wings. It is also possible in this mechanism to change the phase difference between the fore and aft wings β by changing the phase difference between the rotational motion of the front / rear gears. The phase difference can be controlled in 30 degrees increments in the range of 0-360 [deg]. With respect to the feathering angle, there is a mechanism to limit the movable range of the feathering (Fig. 1-d blue squares), and the horizontal attitude is defined as 0 [deg], and the case of where the trailing edge of the wing is located over the leading edge is defined as negative feathering angle, while the case of where the trailing edge of the wing is located under the leading edge is defined as positive feathering angle. The feathering angle can be controlled in 10 degree increments in the range of -90~+90 [deg] and is passively controlled by the aerodynamic force acting on the wing surface. The flapping to the downward (downstroke) leads to negative feathering angle due to the pressure increase on the lower surface of the wing and the feathering angle leads to the minimum value, while the flapping to the upward (upstroke) leads to positive feathering angle due to pressure increase on the upper surface of the wing and the feathering angle leads to the maximum value.

The reference length is defined as 30 [mm] which is the chord length of the single wing and the reference velocity is defined to 1382 [mm/s] which is the averaged flapping velocity at the wing-tip. Then, the Reynolds number becomes 2741. This experiment was performed under the constant output voltage which is based on the flapping frequency of about 3 [Hz] at the range of the feathering angle ± 20 [deg] and the phase difference 90 [deg]. In all cases, the flapping frequency is roughly in the range of 2.45-3.12 [Hz].

C. Visualization of flowfield via particle image velocimetry analysis

A flowchart for visualization of flowfield is shown in Fig. 2. A high speed camera was used to take sequential images in the enclosed region with oil mist as tracer particles and Nd: YAG laser as a light source as shown in Fig. 2.a, and Particle Image Velocimetry (PIV) is used to visualize the flowfield around the tandem flapping wing object. The PIV is one of the fluid measurement method which can obtain instantaneous velocity field without any probe. The tracer particle on the flowfield is visualized by the laser sheet. The sequential images are created by shooting this flowfield with a high-speed camera. The displacement vector (Δx, Δy, Δz,) of the particle for a small time period Δt between two frames is obtained by image processing. Then, the local velocity vector of the flow is calculated as $v_x \cong \Delta x / \Delta t$. Since oil mist is used as tracer particles, it is possible to calculate the velocity of the flowfield by using the brightness distribution in the images as shown in Fig. 2.b. In this research, Optical flow method [11] is used as the PIV analysis method, which is a method often used in the department of computer vision, pattern recognition and robot

vision. In the optical flow method, following optical flow equation is constructed under an assumption that the brightness on the image of the object does not change between consecutive frames.

$$I(x, y, t) = I(x + \Delta x, y + \Delta y, t + \Delta t) \tag{2. 2}$$

where $I(x, y, t)$ is the brightness at the coordinates of (x, y) at time t and $I(x + \Delta x, y + \Delta y, t + \Delta t)$ is the brightness at the coordinates of $(x + \Delta x, y + \Delta y)$ at time $t + \Delta t$. Taylor expansion of the right side gives the following equation.

$$I(x + \Delta x, y + \Delta y, t + \Delta t) = I(x, y, t) + \frac{\partial I}{\partial x}\Delta x + \frac{\partial I}{\partial y}\Delta y + \frac{\partial I}{\partial t}\Delta t + \cdots \tag{2. 3}$$

From the equations of (2.2) and (2.3), the following equation is obtained.

$$\frac{\partial I}{\partial x}\Delta x + \frac{\partial I}{\partial y}\Delta y + \frac{\partial I}{\partial t}\Delta t + \cdots = 0 \tag{2. 4}$$

By ignoring the higher order terms and dividing the equation by Δt, the following optical flow equation is derived.

$$\frac{\partial I}{\partial x}\frac{\Delta x}{\Delta t} + \frac{\partial I}{\partial y}\frac{\Delta y}{\Delta t} + \frac{\partial I}{\partial t} = 0 \tag{2. 5}$$

$$\frac{\partial I}{\partial x}v_x + \frac{\partial I}{\partial y}v_y + \frac{\partial I}{\partial t} = 0 \tag{2. 6}$$

where $\Delta x/\Delta t$ represents the flow velocity component in the x direction v_x and $\Delta y/\Delta t$ represents the flow velocity component in the y direction v_y. Since there are two unknowns (v_x and v_y) and one equation (2.6), flow velocity distribution cannot be obtained only the optical flow equation. Farneback method [12] is used to solve this problem. In the Farneback method, the displacement amount can be estimated by polynomial approximation of the surrounding brightness values by the weighted least squares method.

Ensemble average is used to obtain refined distributions. Since PIV measurement is conducted under unsteady flowfield, there is a problem of data error of PIV analysis at some regions. In the PIV measurement, it is necessary to take images of moving particles inside the flow while the particles are excluded from the surroundings of the wing by the movement of the flapping wings, and sparse particle area are generated in the flowfield. Therefore, the data error of PIV analysis occurs at some regions. To obtain refined distributions, the velocity vector is collected from 13 flapping cycles by averaging the velocity data at each flapping phase θ as shown in Fig. 2.c. In addition, the distribution is averaged to reduce the calculation cost for extracting vortex structures (Fig. 2.d).

The vortex structure is important to understand the mechanism for generating aerodynamic forces in flight of the flapping wing object. The vorticity distribution is calculated by the following equation.

$$\omega = \frac{dv_y}{dx} - \frac{dv_x}{dy} \tag{2. 7}$$

where positive vorticity values correspond to counterclockwise vortices while negative vorticity values correspond to clockwise vortices (Fig. 2.e).

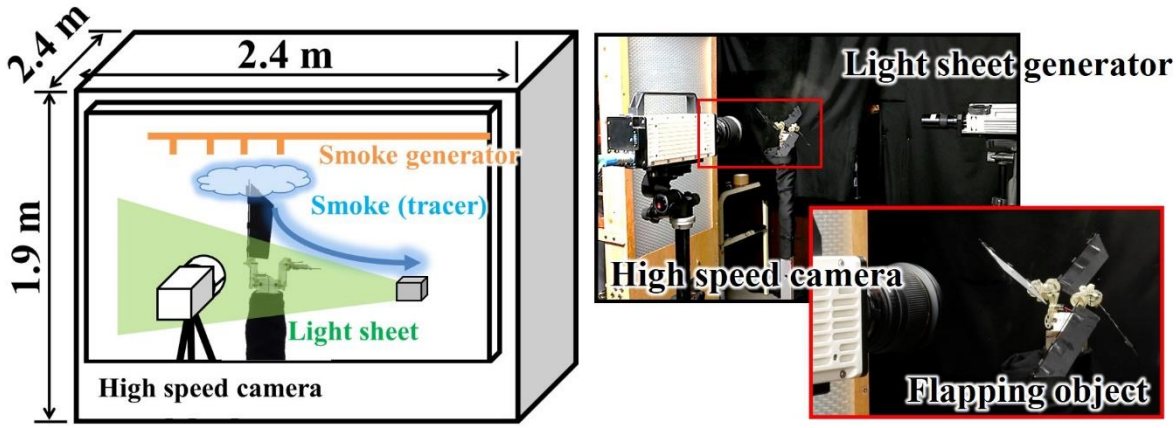

a. Experimental room (left: overview, right: picture)

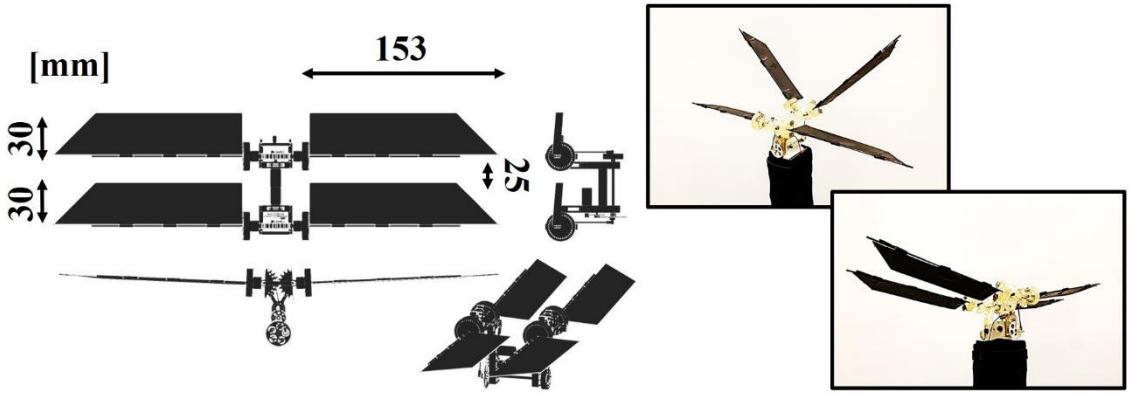

b. Tandem flapping object (left: overview, right: pictures)

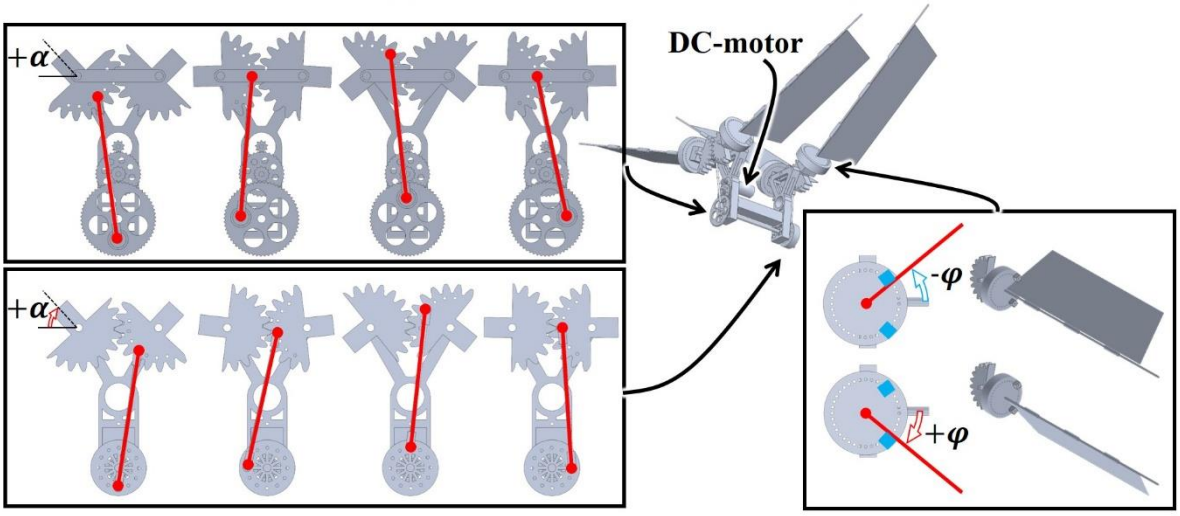

c. Phase difference variable system (upper: front view, lower: rear view)

d. Feathering angle variable system

Fig. 1 Experimental Equipment

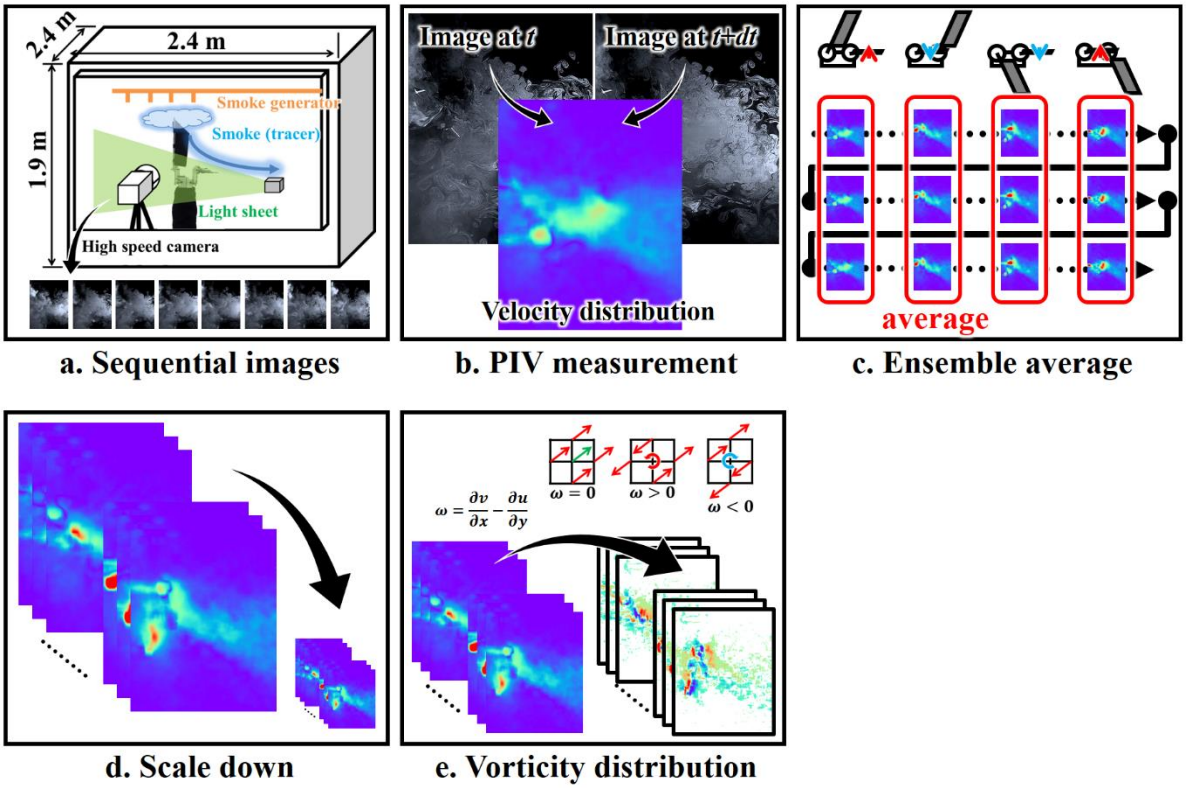

Fig. 2 Flow Visualization Approach

III. Reconstruction of Major Vortex Structure Method I

In this section, the developed Reconstruction of major Vortex Structure method I (RVS- I) is defined.

A. Outline of the reconstruction process of the major vortex structures

The visualization of the vorticity distribution is important for understanding the flowfield of the flapping wing object. However, it is difficult to understand the detailed flow physics from the vorticity distributions obtained via PIV measurement due to the data error or noisiness in the flowfield. Therefore, in this research, we develop a reconstruction method of major vortex structures I (RVS-I) as a postprocessing method of PIV analysis for the purpose to assist the physical understanding of the vortex structures. In this method, vorticity distributions in spatial two-dimension (x, y) and temporal one-dimensional (t) obtained by PIV analysis are considered as data arranged in three-dimensional space (x, y, t) as shown in Fig. 3-a. Then the visualization area is restricted by setting an appropriate threshold value for the vorticity magnitude (Fig. 3.b). In this restricted visualization, there are still many errors while major vorticity structures can be clearly confirmed. Therefore, it is considered that setting of the threshold value is an important parameter for the extraction of vortex trajectory. Then, an ideal path as a vortex trajectory is extracted through the vortex center graph (Fig. 3.c) from the restricted visualized region (Fig. 3.d). Next, the extracted vortex trajectory is removed from the original vortex distribution (Fig. 3.f), and then another ideal path as a vortex trajectory is extracted from the remaining vortex distribution. This process is iterated to extract multiple trajectories of dominant vortices. The extraction of the multiple trajectories is separately applied to the clockwise vortex distribution and the counterclockwise vortex distribution. Finally, the reconstruction of the distribution of dominant vortices is executed by using the information of the extracted vortex trajectories as well as the strength of the vortices (Fig. 3.g, Fig. 3.h).

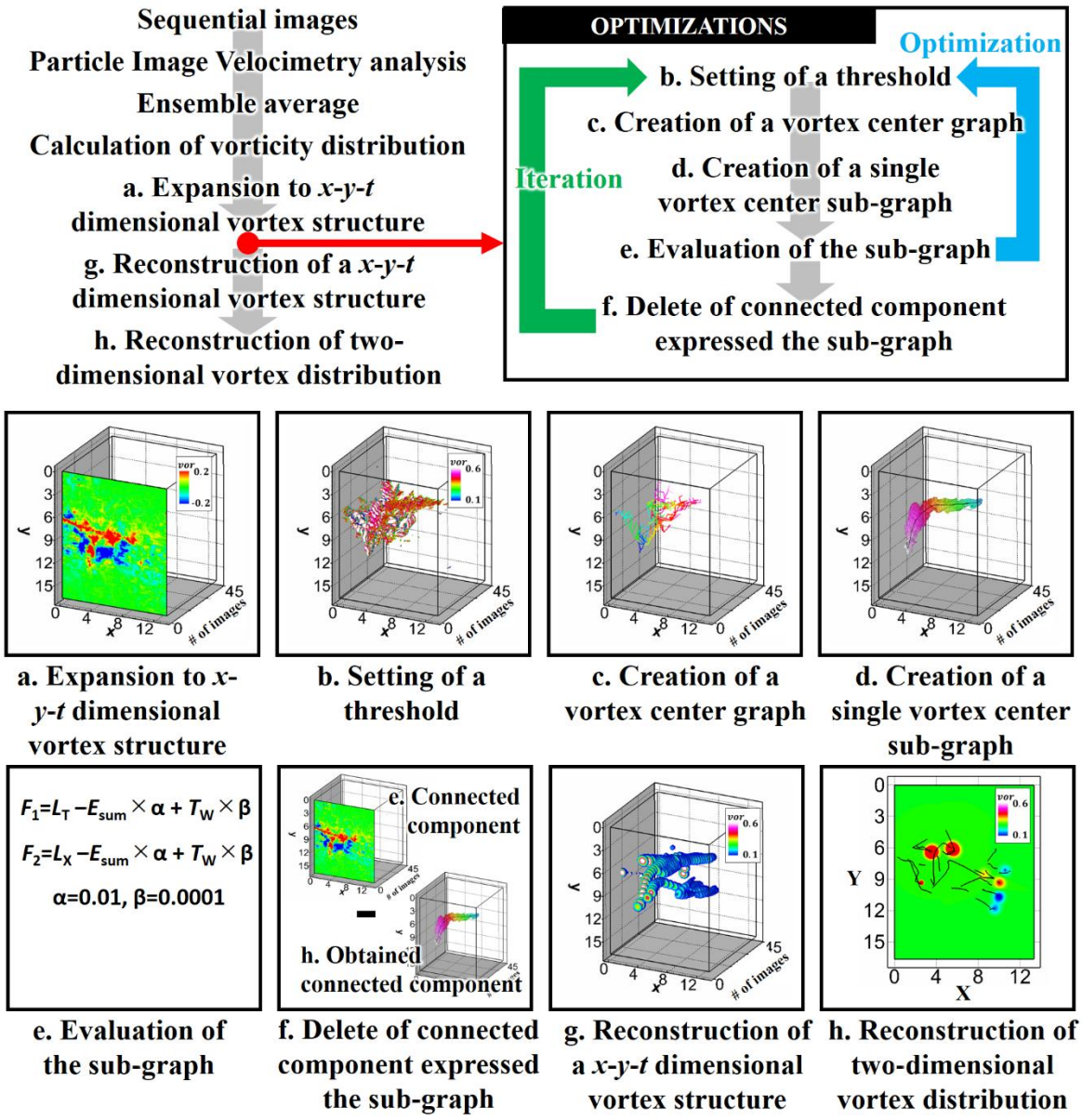

Fig. 3 Flowchart of the Reconstruction Process of Major Vortex Structures

B. Appropriate threshold and vortex trajectory

The appropriate threshold value is determined by solving the optimization problem of (3.1) or (3.2).

$$Maximize \quad F_1 = L_T - \alpha_1 E_{sum} + \beta_1 T_\omega \tag{3. 1}$$

$$Maximize \quad F_2 = L_X - \alpha_2 E_{sum} + \beta_2 T_\omega \tag{3. 2}$$

$$E_{sum} = \sqrt{\frac{\sum_{t=1}^{L_T} (err)^2}{L_T}} \tag{3. 3}$$

where L_T is the length of the vortex trajectory to the *t* direction (sequential number of images) and L_X is the length of the vortex trajectory in the *x* direction (horizontal direction). Large L_T means that the vortex trajectory has strong vorticity for a long time while large L_X means that the vortex trajectory has strong vorticity for a long distance to the x direction. E_{sum} represents the smoothness of the vortex trajectory, which is expressed by RMSE of the difference *err* between the predicted value from the backward differencing and the actual value as Eq. (3.3). Smaller E_{sum} means smoother vortex trajectory which can be considered as correct one in physical sense. α_1 and α_2 are weighting factors for E_{sum} and set to a small value of 0.01. T_ω is the absolute value of the threshold set for restricting the visualization region. This term is set to define the optimal solution to one point and not to delete the connected component of the other vortex trajectory in process Fig. 3.f. Large T_ω means that the visualization region is strongly restricted. β_1 and β_2 are weighting factors for T_ω and set to 0.0001 which is smaller than α_1 and α_2. A schematic diagram of this algorithm is shown in Fig. 4.

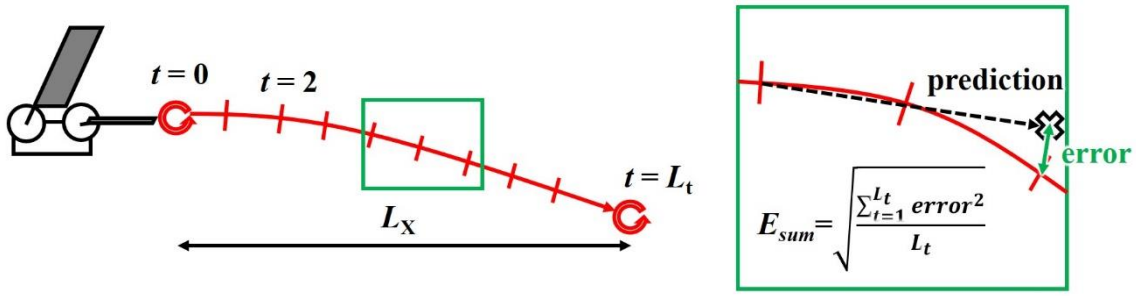

Fig. 4 Objective Function for Vortex Trajectory

C. Extraction of one vortex trajectory

In the present method, tree structured graph representing vortex trajectories are created by a Best Connected Component Graph (RVS-BCC) method. After that, single sub-graph representing vortex trajectory is created by a Greedy and Smooth Sub-graph (RVS-GSS) method from the tree structured graph.

In RVS-BCC (Fig. 5), two-dimensional connected components are created in the *x*, *y* cross section for all image numbers in the *t* direction. Then, the position with the strongest vorticity in each connected component is plotted. After that, the overlapped regions of the connected components are searched at sequential time *t* and *t*+1 and connected edges are created between the overlapped regions. The tree structured graph representing vortex trajectories are created by repeating this process from the start time to the end time. There is a similar method called Thinning Algorithm [13] and a persistence-based method[14], which was initially based on Ref. [15] and provides theoretical guarantees[16]. Thinning algorithm can create a line image with one pixel width. Therefore it can create a tree structured graph from a connected component. However, since there is no physical meaning in the Thinning Algorithm, we developed the present method of RVS-BCC. Fig. 5.b, Fig. 5.c and Fig. 5.d indicate the examples of the connected edges from *t*=T to *t*=T+1, from *t*=T+1 to *t*=T+2, and from *t*=T+2 to *t*=T+3, respectively.

In RVS-GSS (Fig. 6), a reference point and reference edges are created from the tree structure graph. The reference point is defined as a position of the strongest vorticity in the tree structured graph. The reference edges are defined as the connected edges between the reference point and its neighboring points. The coordinates of the neighboring point of the reference edge can be predicted by forward difference method or backward difference method. A vortex trajectory is created by selecting the closest one with the predicted coordinate by a greedy method. The vortex trajectory is created for each reference edge by repeating this process until to reach both of the start time and end time of the connected component. Finally, a vortex trajectory with the smallest E_{sum} is selected from the vortex trajectories. There is a similar method called shortest path algorithm. The shortest path algorithm can create the shortest sub-graph with single path between the start time and the end time of the connected component. However, Fig. 6.b.3 is the vortex trajectory obtained by the shortest path algorithm while Fig. 6.b.1 is the correct vortex trajectory from the viewpoint of physics. Since the shortest path algorithm can't get the correct sub-graph, we developed the present method of RVS-GSS which can select the correct vortex trajectory.

Since the optimization problem for searching the optimum threshold is a discontinuous / nonlinear optimization problem, it is difficult to obtain its exact optimal solution. Therefore, firstly, a Brute Force method is used to get a global optimal point. Then, the Brent method [17] is used to get a detailed optimal point by local optimization method surrounding the global optimal point.

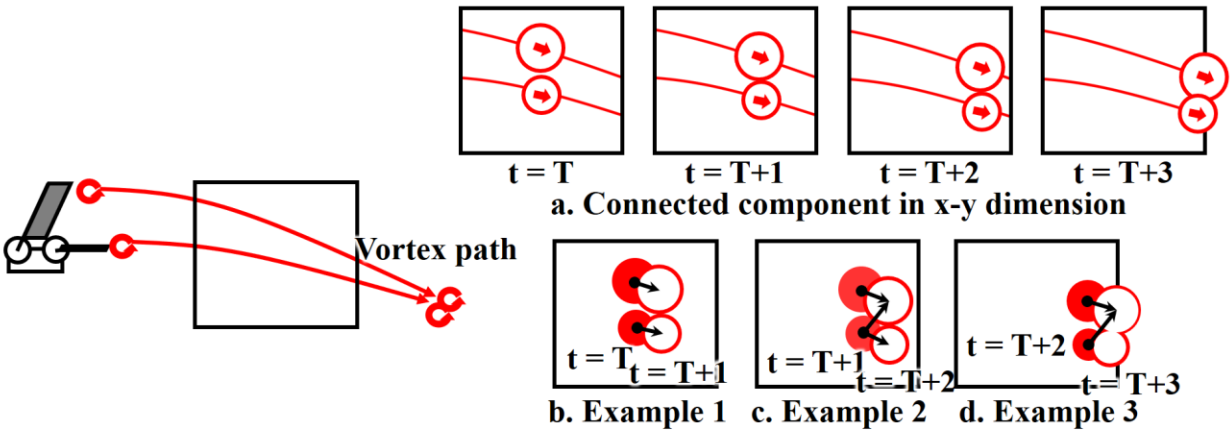

Fig. 5 Best Connected Component Graph (RVS-BCC) Method

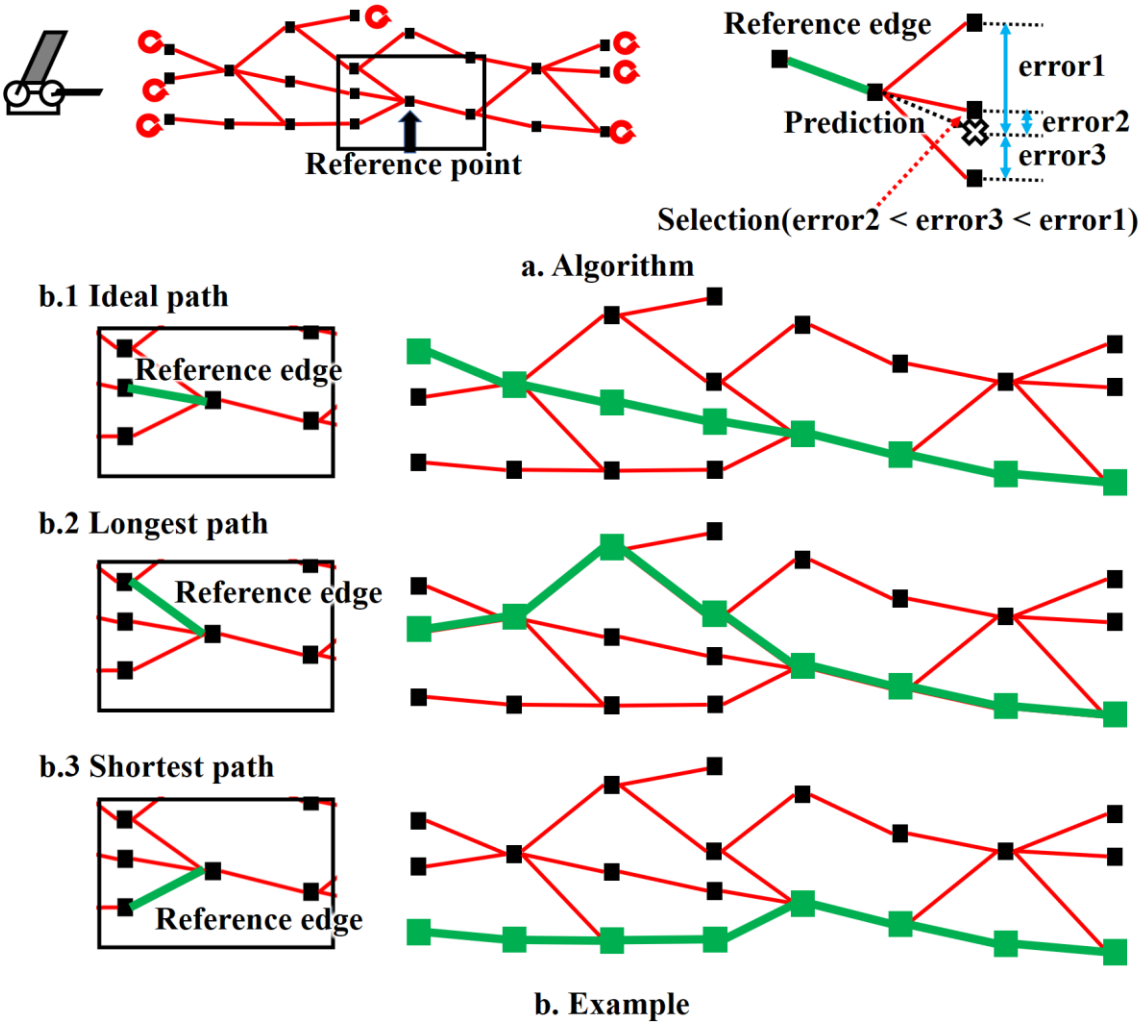

Fig. 6 Greedy and Smooth Sub-graph (RVS-GSS) Method

D. Reconstruction of major vortex structures (Fig. 7)

The vortex center position can be obtained by the previous process, and the vorticity at the vortex center position can be obtained from the vorticity distribution. Therefore, the reconstructed vorticity distribution can be obtained by defining the vorticity around the dominant vortices. Here, it is assumed that the vorticity around a vortex can be represented by a Gaussian function and approximated by the following equation.

$$\overline{\omega} = f e^{-2\frac{r^2}{w^2}} \tag{3. 4}$$

where f represents the vorticity of the vortex center, r represents the distance from the vortex center, and w represents the width of the Gaussian function (2σ). It is assumed that w is related to the vorticity of the vortex center f and approximated by the following equation of the even function.

$$w = IV_1 f^2 + IV_2 \tag{3. 5}$$

where IV_1 and IV_2 represent independent parameters. The vorticity distribution is temporary determined in all x, y, t by setting w for each vortex through setting of IV_1 and IV_2. Here, the error between the true vorticity distribution and the temporary determined vorticity distribution is represented by the following equation.

$$\overline{\omega}_{(x,y),t} = \sum_{n=1}^{n_t} f_{t,n}\, e^{-2\frac{r_{(x,y),t,n}{}^2}{w_{t,n}{}^2}} \tag{3. 6}$$

$$e_{ss} = \sum_{t=0}^{t_{max}} \sum_{y=0}^{y_{max}} \sum_{x=0}^{x_{max}} \left(\overline{\omega}_{(x,y),t} - \omega_{(x,y),t}\right)^2 \tag{3. 7}$$

where n_t represents the number of extracted major vortex centers at t and e_{SS} represents the sum of square error between approximated vorticity distribution $\overline{\omega}_t$ and the true vorticity distribution ω_t. IV_1 and IV_2 are determined so as to minimize the error equation to obtain approximated vorticity distribution.

$$Minimize \quad e_{ss} = \sum_{t=0}^{t_{max}} \sum_{y=0}^{y_{max}} \sum_{x=0}^{x_{max}} \left(\overline{\omega}_{(x,y),t} - \omega_{(x,y),t}\right)^2 \tag{3. 8}$$

This optimization problem can be treated as a nonlinear least squares problem and this nonlinear least squares problem is solved by Levenberg-Marquardt algorithm [18].

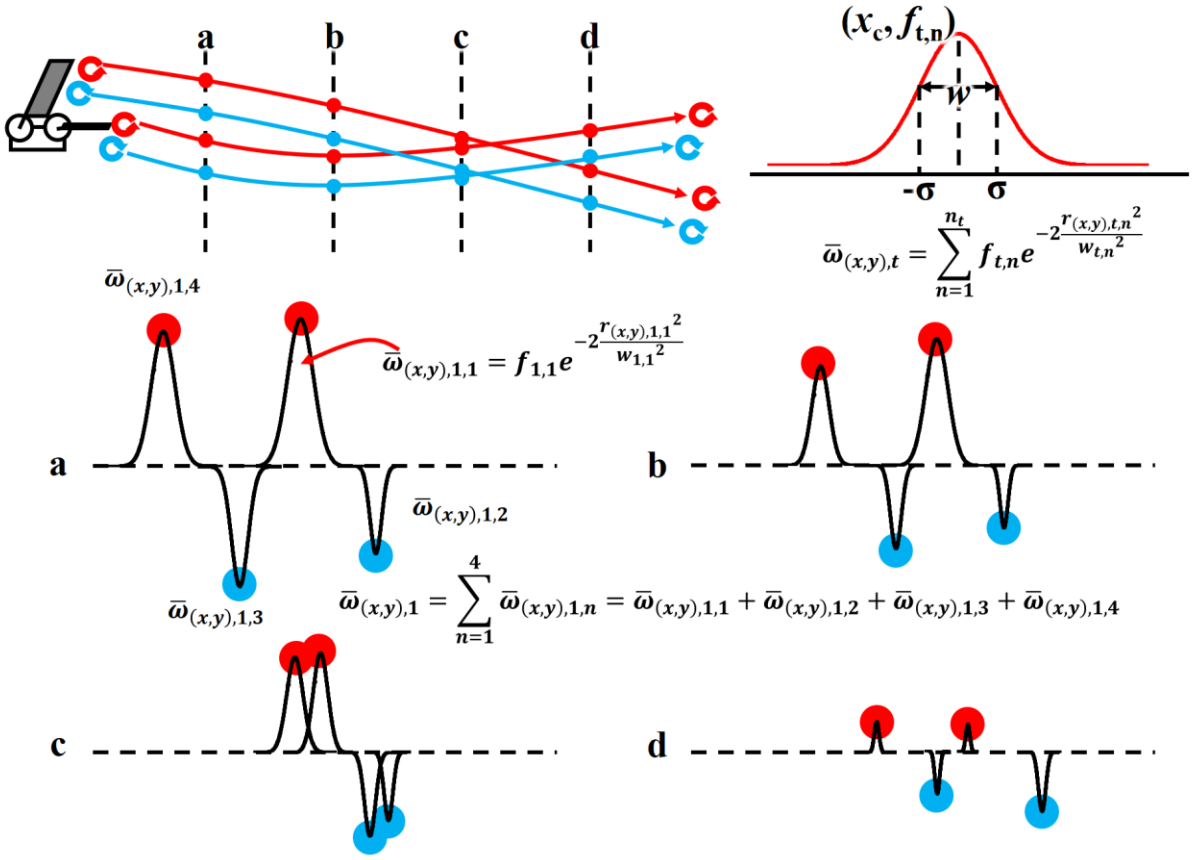

Fig. 7 Reconstruction of Major Vortex Structure Method

E. Results and Discussion

In the process of the proposed vorticity trajectory extraction method, the threshold value is treated as a design variable to limit the visualization region of the vorticity distribution and Eq. (3.1) or Eq. (3.2) is used as the objective function to obtain the optimum vorticity trajectories for reconstruction. The design range of the threshold value was set to 0.1~0.6 for positive vorticity and -0.6~-0.1 for negative vorticity. Then, the optimization process for the extraction of the vorticity trajectory was performed for the positive vorticity distribution and the negative vorticity distribution separately. Firstly, the optimization process for the positive vorticity distribution was performed 10 times. After that the optimization process for the negative vorticity distribution was also performed 10 times. The vorticity reconstruction algorithm was applied to two cases of feathering angle of 20 [deg] and phase difference of 150 [deg] (FA20-PD150) and of feathering angle of 40 [deg] and phase difference of 90 [deg] (FA40-PD90). These conditions respectively gave the maximum thrust force and characteristic induced flow that were discussed in [9]. Fig. 8 and Fig. 9 show vortex distributions/trajectories in (x, y, t) dimension obtained by the present reconstruction algorithm. Fig. 10, Fig. 11, Fig. 12 and Fig. 13 show vortex distributions in (x, y) dimension obtained by the present reconstruction algorithm.

Fig. 8 shows vortex distributions of the FA20-PD150 (tandem flapping wing object with 20 [deg] of feathering angle and 150 [deg] of phase difference) in (x, y, t) space. a-d represent vorticity distributions extracted from PIV data and e-h represent reconstructed vorticity distributions. The visualization region is limited less than -1.0 in a, less than -0.5 in c, e and g, greater than 1.0 in b, and greater than 0.5 in d, f and h. The vortex trajectories of e and f are optimized by Eq. (3.1) while that of g and h are optimized by Eq. (3.2). The dominant vorticity structures can be clearly observed by strongly limiting the visualization region using the vorticity threshold (Fig. 8-a, Fig. 8-b), while the information of small vortices has been lost. Therefore, the appropriate setting of the threshold value is important for extraction of the trajectories of small vortices. It can be confirmed from the vorticity distributions of Fig. 8-e ~ Fig. 8-h that there are no extra vortex structures while several weak vortices can be extracted in the region of $X > 5.0$. On the other hand, it is difficult to reconstruct the vortex distribution around the wing ($X < 0.5$) since the flowfield around the wing was

not measured clearly due to the dead angle of the light source or sparse smoke distribution. Fig. 9 shows vortex distributions of the FA40-PD90 case (tandem flapping wing object with 40 [deg] of feathering angle and 90 [deg] of phase difference) in (x, y, t) space. In Fig. 9-e-h, small vortices behind the object (X > 5.0) were clearly reconstructed while large vortices around the wing could not be reconstructed by the same reason with Fig. 8.

Fig. 10, Fig. 11, Fig. 12 and Fig. 13 show the vortex distributions in (x, y) space obtained by the present vorticity reconstruction algorithm. Fig. 10 and Fig. 11 are the flow visualization around the FA20-PD150 case, while Fig. 12 and Fig. 13 are the flow visualization around the FA40-PD90 case. Fig. 10 and Fig. 12 correspond to the downstroke of the fore-wing, while Fig 11 and Fig. 13 correspond to the upstroke of the fore-wing. In these figures, a, e, i and m indicate ensemble averaged velocity distributions, b, f, j and n indicate ensemble averaged vorticity distributions, c, g, k and o indicate reconstructed vorticity distribution optimized by Eq. (3.1), and d, h, l and p indicate reconstructed vorticity distribution optimized by Eq. (3.2). The flow velocity distribution is visualized by normalizing by the flapping velocity at the wing-tip of the flapping wing object, and it is confirmed from the figures that the flow velocity on the wing-tip equals about 1. It is confirmed that it is difficult to follow the vortex trajectory and to discuss the detailed flowfield from the ensemble averaged vorticity distribution (b, f, j and n) due to those noisiness. On the other hand, it is easy to follow the vortex trajectory and to discuss detailed flowfield from the reconstructed vorticity distributions (c, d, g, h, k, l, o and p). With respect to the vorticity distributions reconstructed by Eq. (3.1), since large L_T means that the vortex trajectories have strong vorticity for a long time, this algorithm can trace the stagnating vortex as seen in (x, y) = (2, 10) of Fig. 10-g. With respect to the vorticity distribution reconstructed by Eq. (3.2), since large L_X means that the vortex trajectory have strong vorticity for a long distance to the x direction, this algorithm can trace the small vortices generated from the wings as seen in x > 5.0 of Fig. 10-h and Fig. 10-l. It is necessary to select appropriate objective function to reconstruct vortex structures as users desire.

In Fig. 10 and Fig. 11 of the FA20-PD150 case, a strong counterclockwise vortex is generated between the fore- and aft wings when the fore / aft wings are crossed due to the downstroke of the fore-wing and the upstroke of the aft wing (Fig. 10-o, (x, y) = (3, 5)). Furthermore, this vortex follows the upstroke of the aft wing and moves to the +y direction (Fig. 11-c, (x, y) = (3, 7)). This counterclockwise vortex and the clockwise vortex generated on the upper surface of the fore-wing (Fig. 11-c, (x, y) = (1, 2)) accelerate the induced flow generated from the fore-wing as shown in Fig. 11-a. This mechanism is schematically shown in Fig. 14.

In Fig. 12 and Fig. 13 of the FA40-PD90 case, a strong counterclockwise vortex is generated when the aft wing is in the downstroke motion (Fig. 13-g, (x, y) = (5, 4)). This vortex moves backward by the induced flow. This counterclockwise vortex and a clockwise vortex generated on the upper surface of the aft wing (Fig. 13-f, (x, y) = (4, 2)) accelerate the induced flow generated from the fore-wing as shown in Fig. 13-e. This mechanism is also schematically shown in Fig. 15.

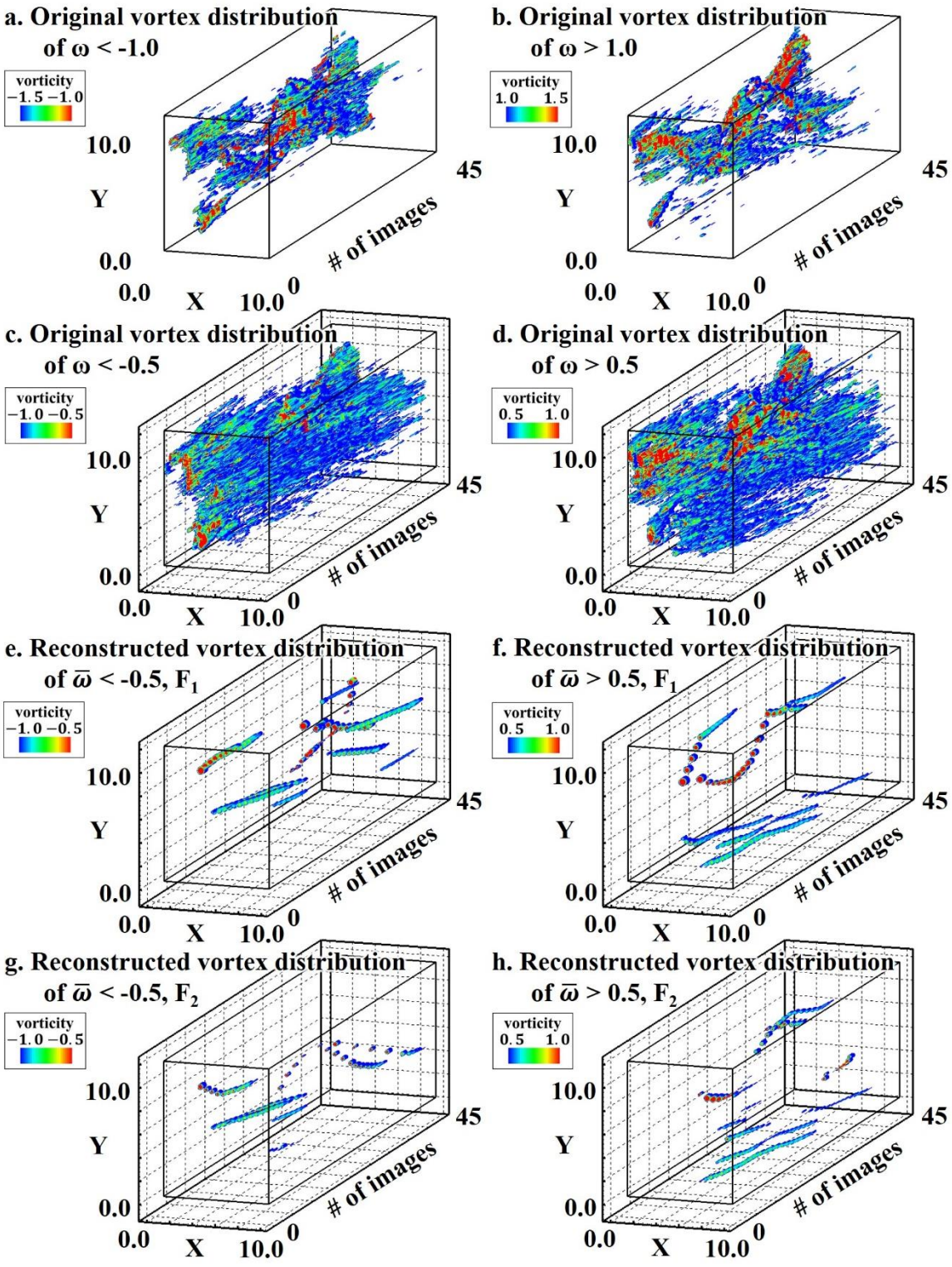

Fig. 8 Vortex Distributions of FA20-PD150 in (*x*, *y*, *t*) Space

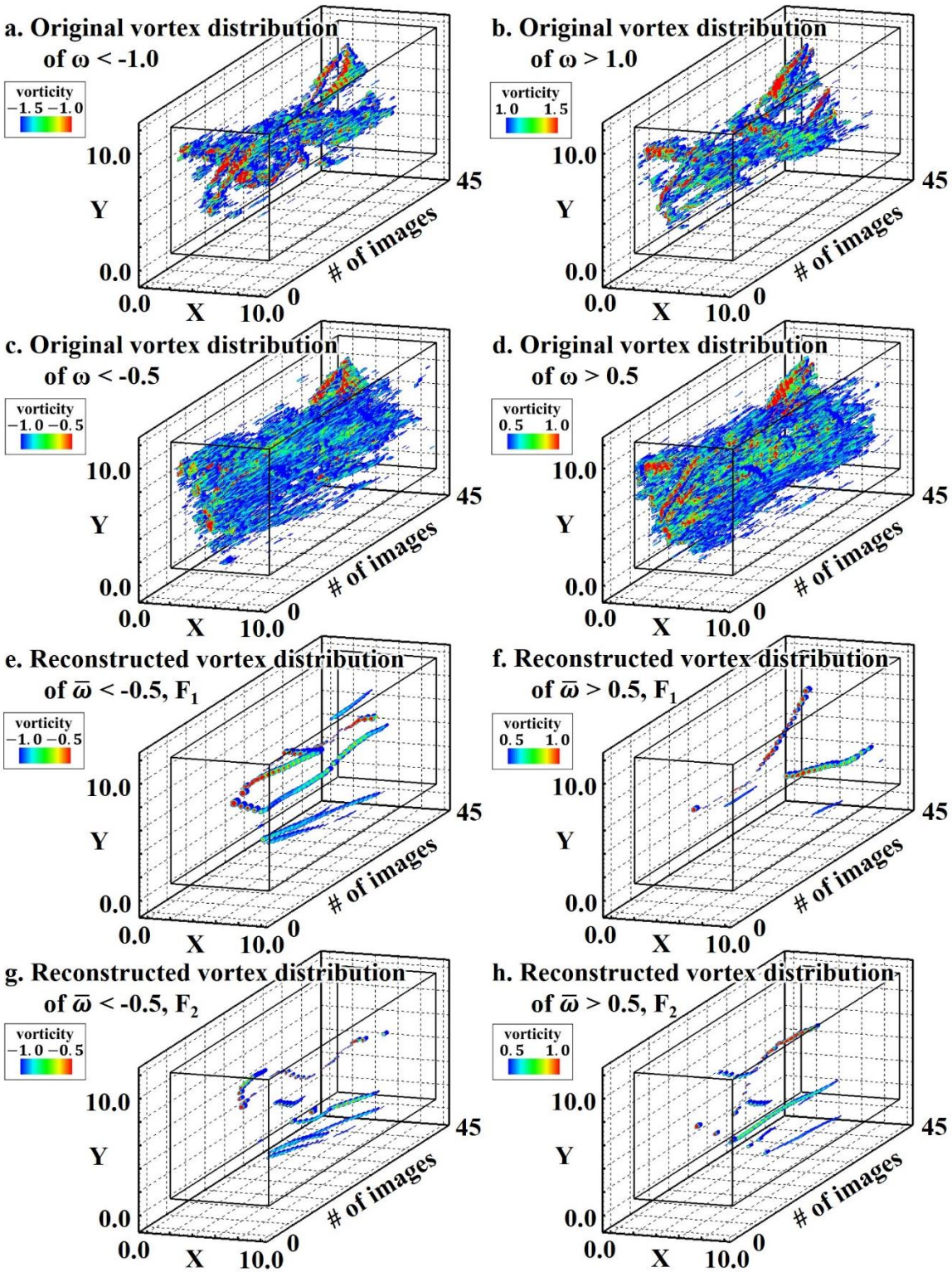

Fig. 9 Vortex Distributions of FA40-PD90 in (*x*, *y*, *t*) Space

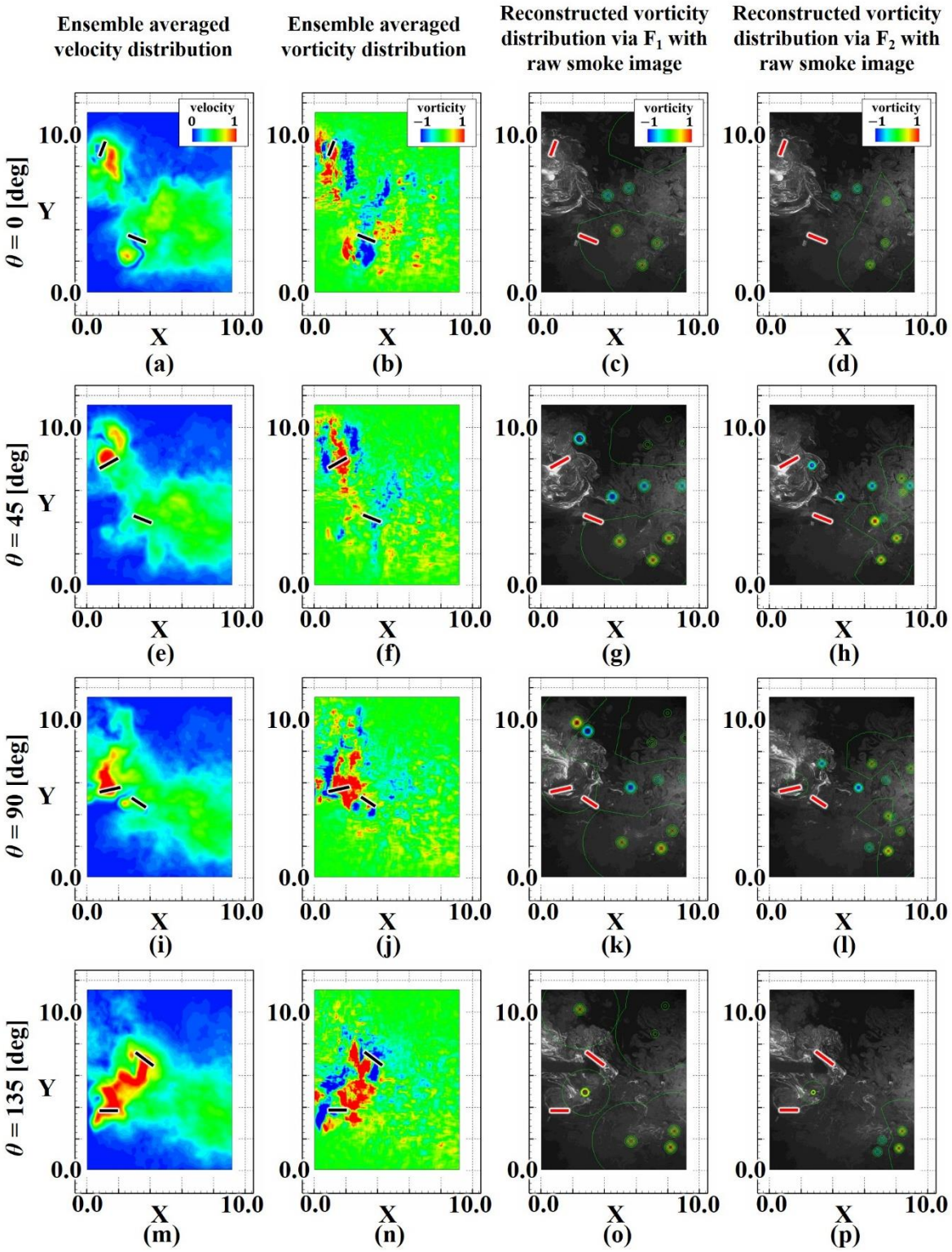

Fig. 10 Vortex Distributions of FA20-PD150 in (*x*, *y*) Space at Downstroke of Fore-wing

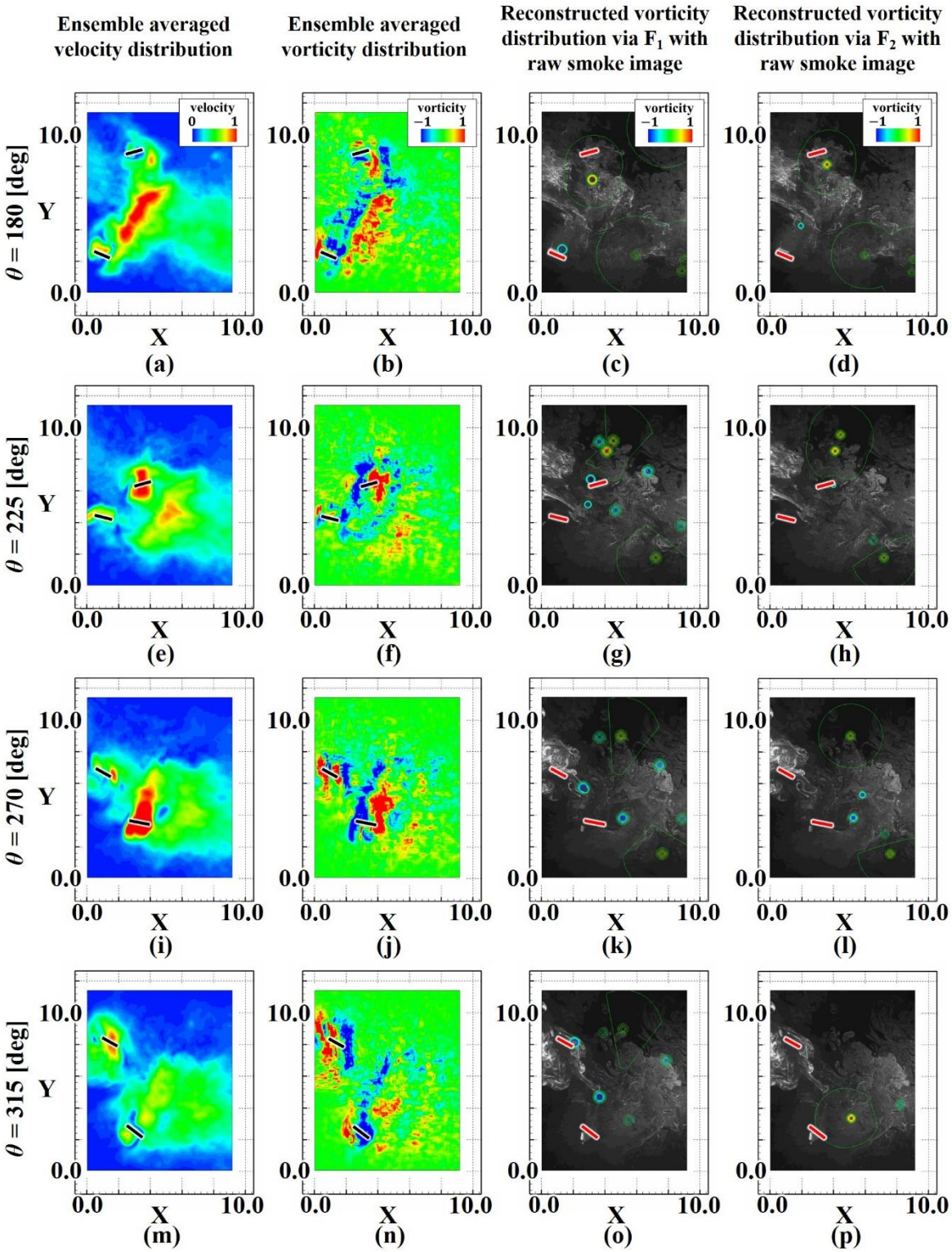

Fig. 11 Vortex Distributions of FA20-PD150 in (*x*, *y*) Space at Upstroke of Fore-wing

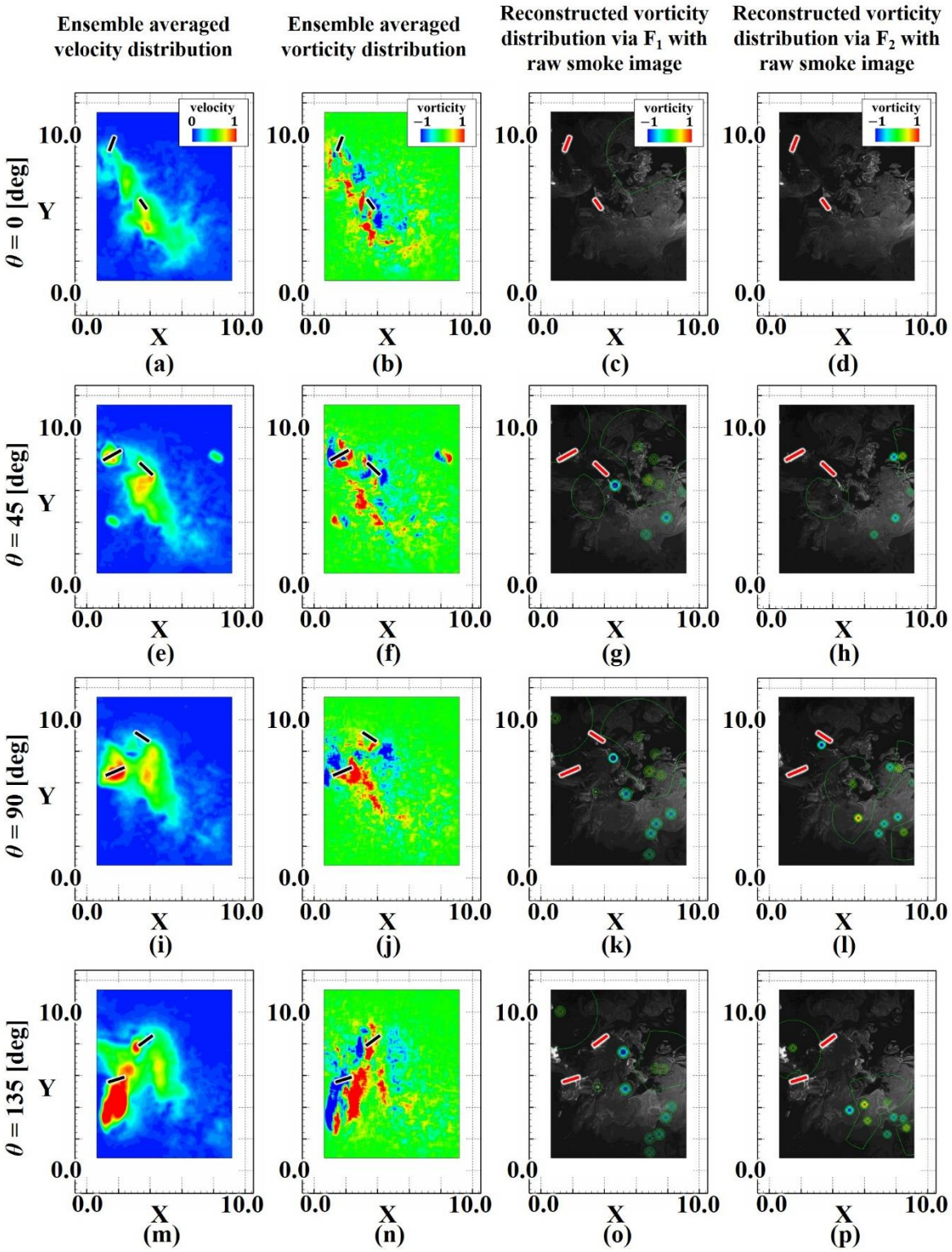

Fig. 12 Vortex Distributions of FA40-PD90 in (x, y) Space at Downstroke of Fore-wing

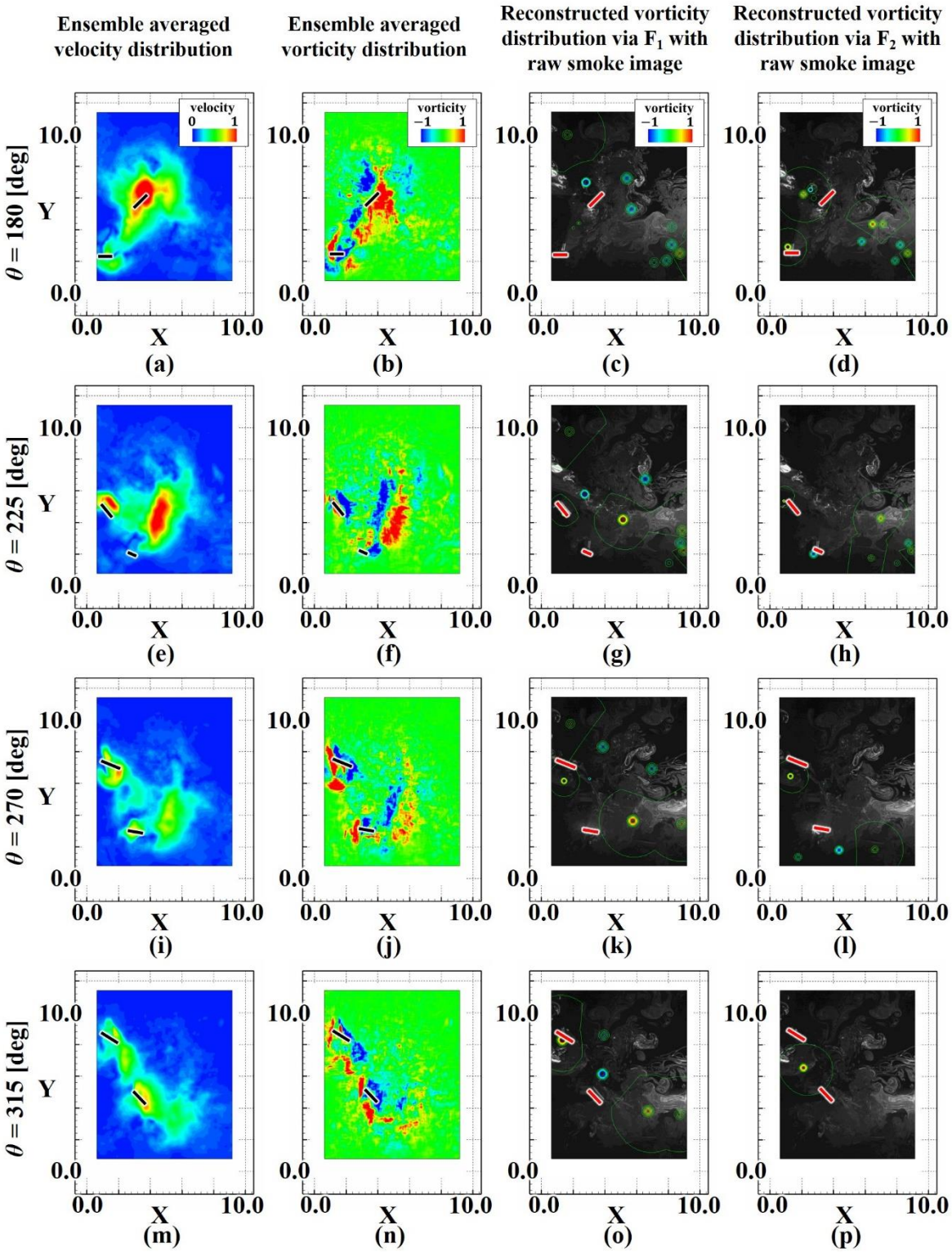

Fig. 13 Vortex Distributions of FA40-PD90 in (x, y) Space at Upstroke of Fore-wing

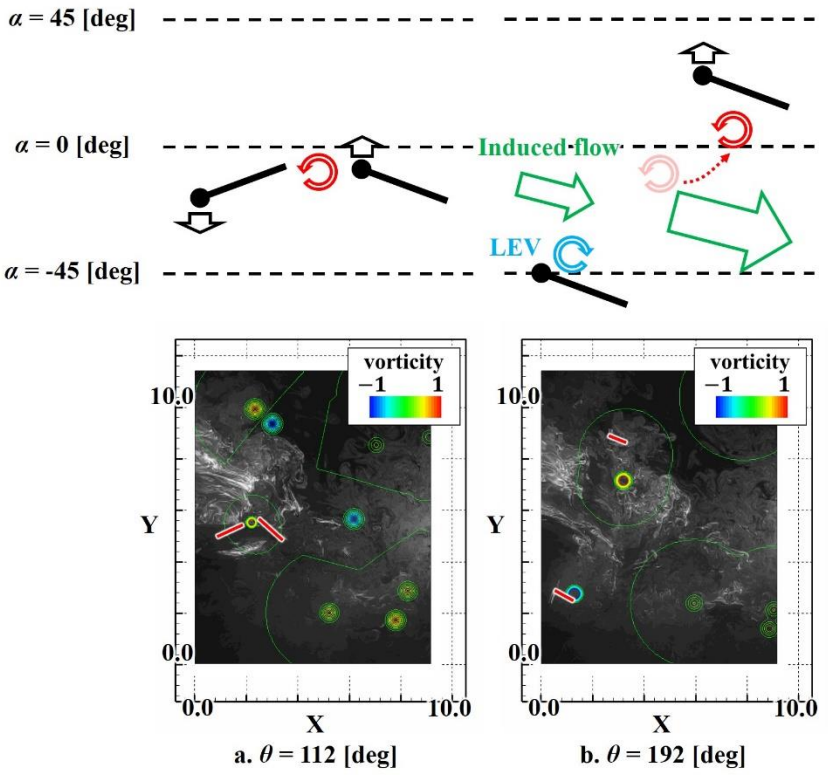

Fig. 14 Induced Flow Mechanism of FA20-150

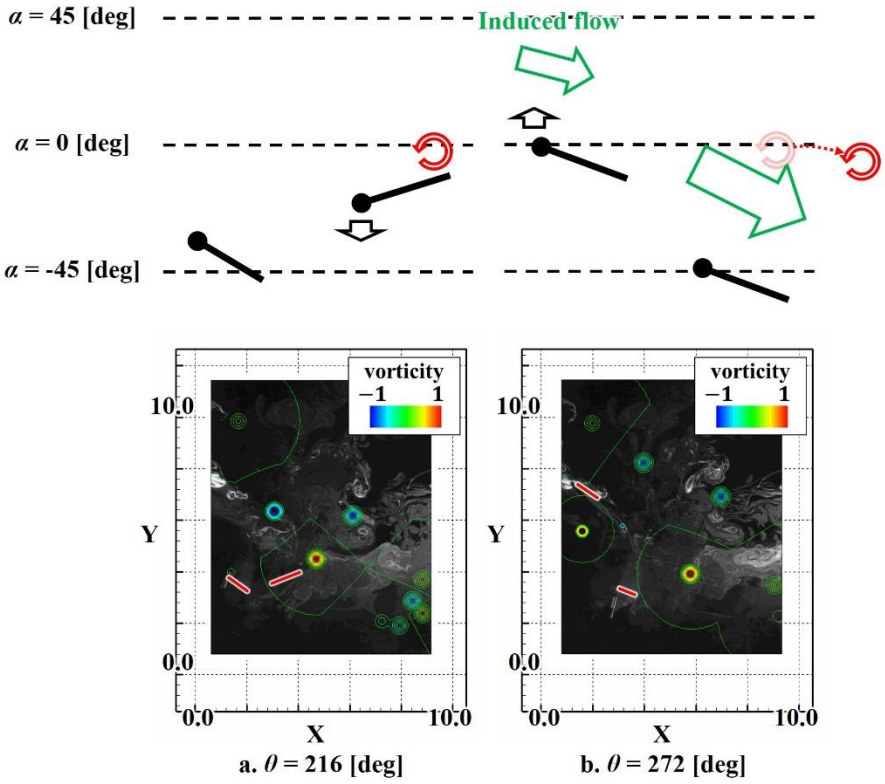

Fig. 15 Induced Flow Mechanism of FA40-90

IV. Reconstruction of Major Vortex Structure Method II

In this section, the developed method for Reconstruction of major Vortex Structure II (RVS- II) is introduced.

A. Outline of the reconstruction process of the major vortex structures in RVS-II

In the RVS-I, vortices are extracted by assuming that important vortices move smoothly and exist for a long distance and for a long time. As a result, several dominant vortices could be extracted and it facilitated the discussion of vortical flowfield. However, a threshold value has to be set to extract the dominant vortex structure. An optimization problem is solved to obtain the appropriate threshold value. Its calculation cost is extremely high since the evaluation of the objective function value requires the consideration of large sized tree structure as well as large sized mesh structure in temporal/spatial dimensions. In addition, since there is only one threshold value to extract one vortex trajectory, it is difficult to accurately capture the vortex at the farfield region. In addition, the vortex moves/generates cyclically in cases with periodic motions such as the flapping wing object. A vortex existing at $t = 0$ may remain at $t = t_{max}$. In the RVS-I, the behavior of periodic vortices cannot be captured, so that some vortex trajectories may become unrealistically short. To solve these problems, the RVS-I was improved for lower-cost and for higher-accuracy. In the improved algorithm, its input data is time-series data of information that move smoothly in space, and its output data is the reconstructed data of the input information. In the case of reconstruction of the vorticity distribution around the flapping wing object, the input data is time series data of vorticity distribution obtained in the visualization of the flowfield (Fig. 1). The RVS-II algorithm can be divided into three steps: determination of the vortex source, extraction of the vortex trajectory, and reconstruction of the vortex structure.

B. Step of determination of vortex source

In the first step of the determination of vortex source, the input time series data (Fig. 16.a) is shaped into a three-dimensional mesh structure (Fig. 16.b) which is called BOX. Then, by setting a threshold value (Fig. 16.c) and executing clustering of the connected components (Fig. 16.d), the vortex structures can be decomposed into several parts which is called SUB-STRUCTURE. The vortex source (SOURCE) is explored for each SUB-STRUCTURE. The summary of the determination of vortex source algorithm is shown in Fig. 17. Fig. 17.a indicates a selected SUB-STRUCTURE. Firstly, the BOX is divided into arbitrary numbers in the time-series direction (Fig. 17.b), the decomposed mesh structure is called SUBBOX and the decomposed vortex structure is called SUBBOX-STRUCTURE. Then, the highest vorticity point for each SUBBOX-STRUCTURE is extracted as a candidate point of SOURCE (Fig. 17.c). Since the object exists on the left side and the vortex moves to the right side in this research, it is considered that the vortex source should be located on the left side and SOURCE is set to the leftmost point among the candidate points (Fig. 17.d). Fig. 17.e indicates enlarged view of a SUBBOX-STRUCTURE with SOURCE.

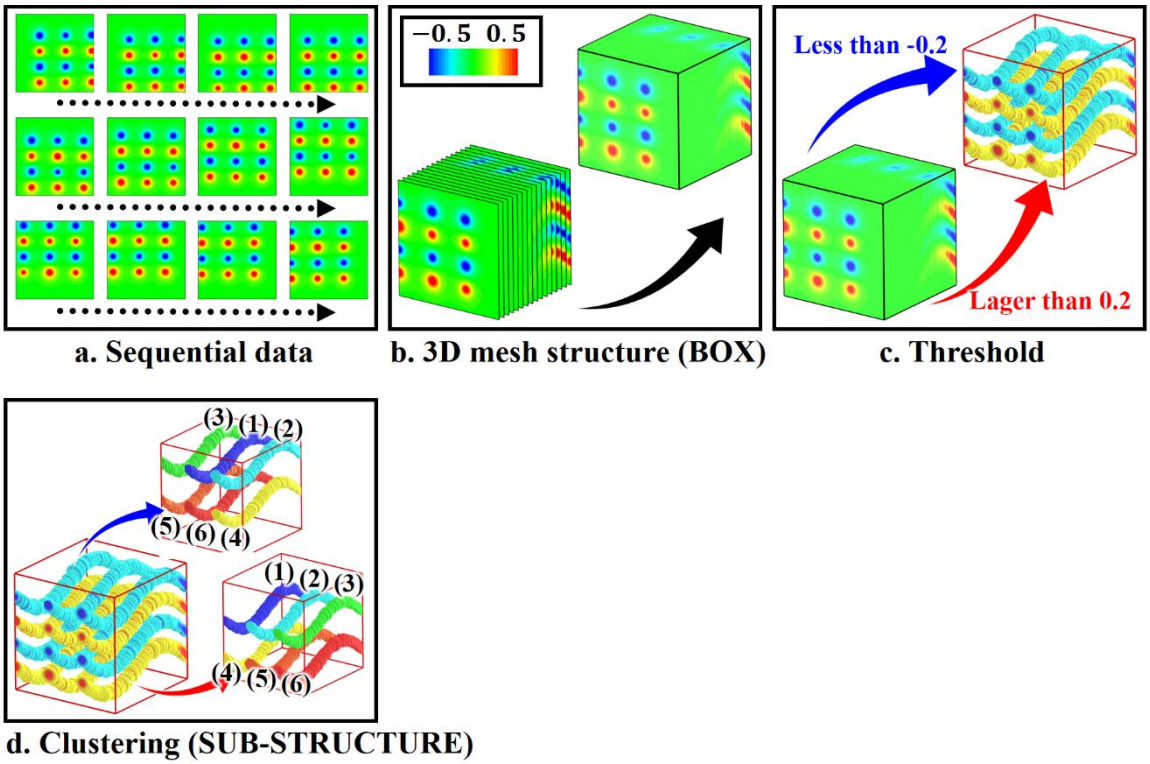

a. Sequential data b. 3D mesh structure (BOX) c. Threshold

d. Clustering (SUB-STRUCTURE)

Fig. 16 Outline of SUB-STRUCTURE

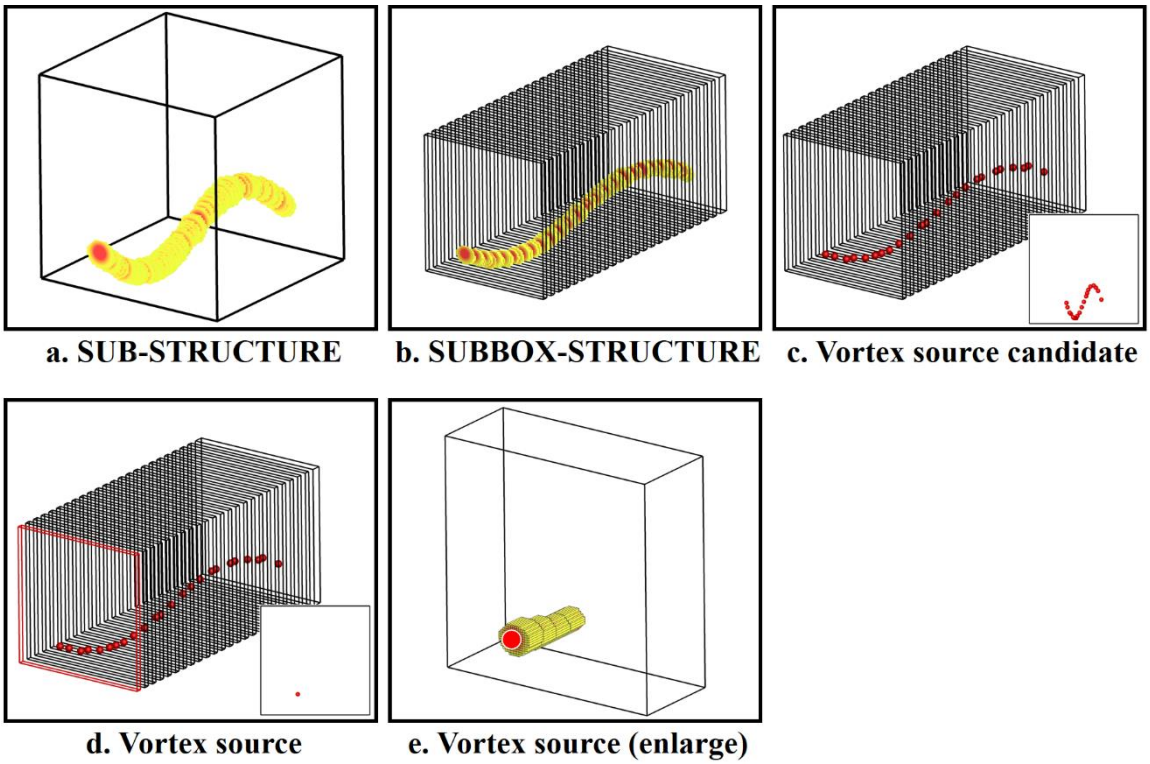

a. SUB-STRUCTURE b. SUBBOX-STRUCTURE c. Vortex source candidate

d. Vortex source e. Vortex source (enlarge)

Fig. 17 Outline of SOURCE

C. Step of extraction of vortex trajectory

Next, local vortex trajectory in SUBBOX are extracted from SOURCE and SUBBOX. The algorithm of the extraction of local vortex trajectory is summarized in Fig. 18. Fig. 18.a and Fig.18.b are respectively BOX and SUBBOX. Fig. 18.c and Fig. 18.d are SUBBOX with detected SOURCE. SUBBOX-STRUCTURE can be obtained by setting a threshold for the SUBBOX (Fig. 18.e) and executing clustering for the connected components (Fig. 18.f). A SUBBOX-STRUCTURE from SOURCE (Fig. 18.g) is selected from the clustered SUBBOX-STRUCTURE, and the following objective function value is evaluated.

$$f = d_{connect}(T_\omega) + \frac{T_\omega - \omega_{min}}{\omega_{max} - \omega_{min}} \tag{4. 1}$$

where $d_{connect}$ is the number of temporal frames a vortex can be connected, which is a function of T_ω. T_ω is the threshold value to be optimized. ω_{min} and ω_{max} are respectively the minimum / maximum values of vorticity magnitude. The second term of the equation represents a non-dimensional value and varies from 0 to 1. Since $d_{connect}$ is an integer value (whose effect if always larger than the second term), the maximization of the function results in the condition giving the longest vortex trajectory. The second term yields the maximum threshold value which gives the largest $d_{connect}$ value. If $f > d_{max}$ (d_{max}: number of maximum frames in a SUBBOX), a vortex trajectory covers the all temporal frames of SUBBOX. In addition, the value of the threshold when maximizing the function is the maximum threshold value satisfying $d_{connect} = d_{max}$, and the SUBBOX-STRUCTURE obtained by the optimum threshold leads the smallest number of vortex elements (Fig. 18.h). If $d_{connect} \neq d_{max}$ when maximizing the function, it means that the object to be tracked no longer exists. Although the objective function is a discontinuous function, it is a convex function without $df/dT_\omega = 0$. Therefore, the optimal solution can be obtained by a ternary search. The local vortex trajectory in SUBBOX can be obtained by creating a vortex center graph via the RVS-BCC algorithm from the obtained SUBBOX-STRUCTURE and creating a vortex center sub-graph via the RVS-GSS algorithm from the vortex center graph. By defining the end point of the local vortex trajectory to the start point of the next SUBBOX, it is possible to extend the vortex trajectory. By iteratively performing above process, it is possible to extend the vortex trajectory to the end of the BOX. It is possible to capture the periodic vortex behavior by executing the same process for the beginning of SUBBOX with the end of the BOX as the SOURCE. Moreover, the threshold value can be set for each SUBBOX in RVS-II, so that the detailed behavior can be captured even if the vorticity magnitude decreases as it propagates to the farfield. In addition, the extraction of vortex trajectory is executed for each local SUBBOX, its computational cost can be drastically reduced. In this algorithm, when there are multiple vortex trajectories in the SUBBOX-STRUCTURE, the single vortex center sub-graph is forcibly connected with another vortex trajectory, and then unrealistic vortex trajectory might be obtained. Therefore, the search domain of a vortex is restricted (Fig. 18.i) as SOURCE is located inside of the restricted domain. Since a local vortex trajectory is searched only in the restricted domain of SUBBOX-RESTRICT, the calculation cost can be drastically reduced. The convergence conditions of the vortex extraction algorithm are as follows: (1) When the vortex outlets from analysis domain. Several pixels on boundary region are considered as the out of analysis domain. (2) When f_{max} (f_{max}: maximum function value of f) is less than d_{max}. It means that the object to be tracked no longer exists. (3) When the specified number of periodic vortex searches is reached. It is necessary to terminate the vortex trajectory which is constantly staying in the same location. By executing the vortex trajectory extraction algorithm for all SUB-STRUCTURE, it is possible to extract multiple vortex trajectories. However, if BOX is very complex data, there will be an enormous number of SUB-STRUCTURE by the clustering of the connected components (Fig. 16.d). Therefore, several number of trajectories are extracted from larger elements size of SUB-STRUCTURE.

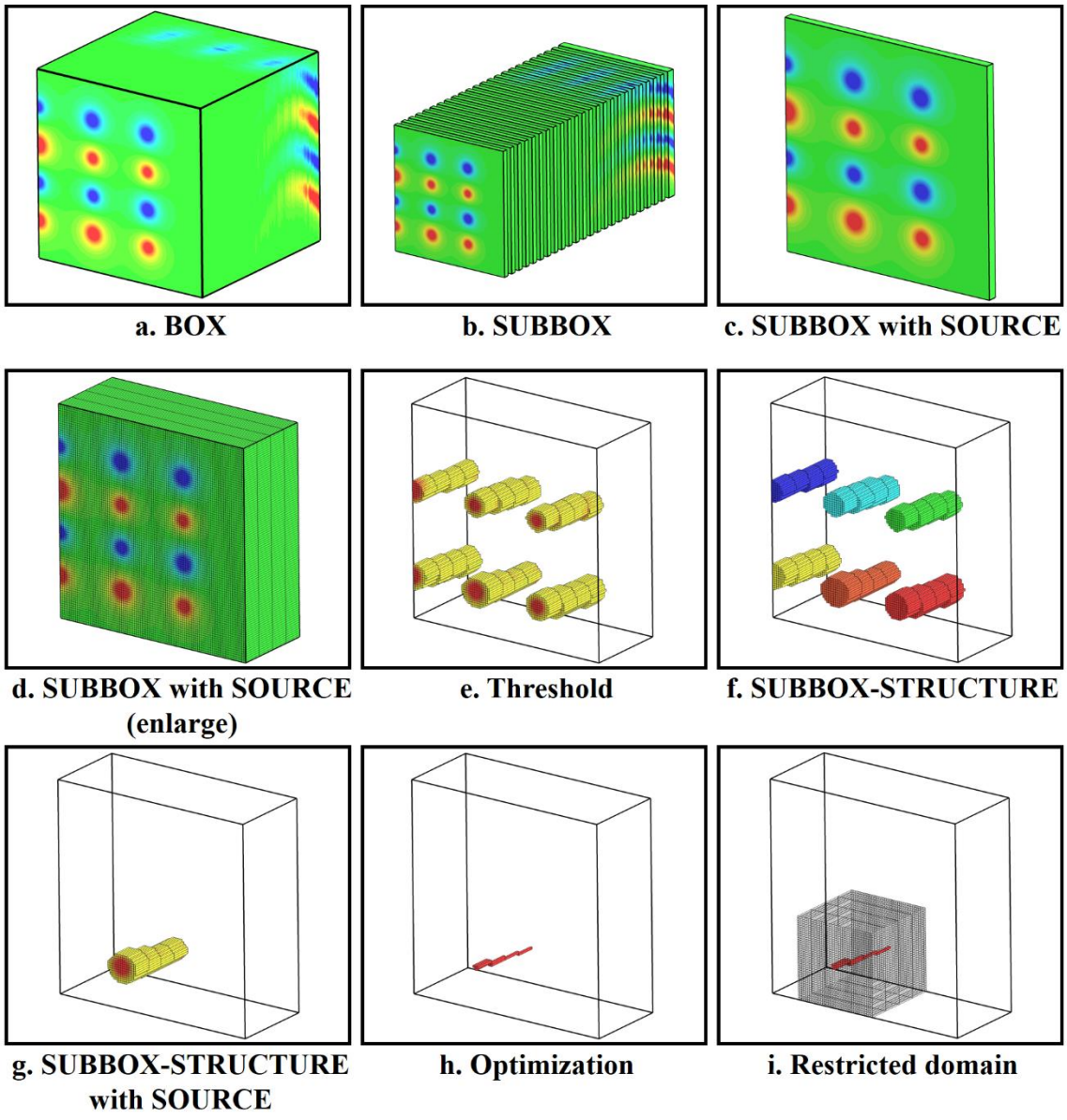

Fig. 18 Outline of Extraction of Vortex Trajectory

D. Step of reconstruction of vortex structure

In this algorithm for the extraction of the vortex trajectory, it can be confirmed that almost same vortex trajectories are obtained, or very short vortex trajectories are generated. Furthermore, when there is an enormous number of vortex trajectories, the computational cost in the reconstruction of vortex structure becomes dramatically expensive. Therefore, the reconstruction algorithm is necessary to be simpler than RVS-I. The distance of arbitrary coordinates (x, y) from a vortex center (x_{nc}, y_{nc}) is given as:

$$r_{x,y,n_c} = \sqrt{(x - x_{nc})^2 + (y - y_{nc})^2} \tag{4. 2}$$

where n_c is the index of the vortex created from one vortex trajectory. The vorticity distribution created by the n_c-th vortex is expressed as follows.

$$\begin{cases} if\, r_{x,y,n_c} < \frac{w}{2}: \\ \qquad \bar{\omega}_{x,y,n_c} = 0 \\ else: \\ \qquad \bar{\omega}_{x,y,n_c} = -2f_{nc}\frac{r_{x,y,n_c}}{w} + r_{x,y,n_c} \end{cases} \tag{4.3}$$

$$\bar{\omega}_{x,y} = \sum_{n_c=1}^{n} \bar{\omega}_{x,y,n_c} \tag{4.4}$$

where w represents a vortex diameter which can be set to an arbitrary constant value. The vorticity distribution generated by multiple vorticity trajectories is expressed as follows.

$$\begin{cases} \bar{\omega}_{pos,x,y} = max\left(\bar{\omega}_{x,y,pos}\right), & pos \in positive\ vortex \\ \bar{\omega}_{neg,x,y} = min\left(\bar{\omega}_{x,y,neg}\right), & neg \in negative\ vortex \end{cases} \tag{4.5}$$

where $\bar{\omega}_{pos,x,y}$ and $\bar{\omega}_{neg,x,y}$ represent the vorticity distribution that has counterclockwise and clockwise vorticity, respectively. The total vorticity distribution is expressed as follows.

$$\bar{\omega}_{x,y} = \bar{\omega}_{pos,x,y} + \bar{\omega}_{neg,x,y} \tag{4.6}$$

The vorticity distribution at a distant position from the vortex center is not accurate. However, the computational cost to reconstruct the vorticity distribution is dramatically reduced compared to RVS-I.

E. Reconstruction of vortex structure for test function

To verify the usefulness of the developed RVS-II algorithm, the vorticity distribution is reconstructed from the test function. An analysis domain is set to $0.0 < x < 1.0$ and $0.0 < y < 1.0$, and a data interval is set to dx=0.01, dy=0.01. In this test function, there are totally 4 vortices; two of them rotate counterclockwise and the other two rotate clockwise. Each vortex moves along x-direction with a constant velocity defined as follows.

$$x_c = \frac{1}{300}t \tag{4.7}$$

With respect to the clockwise vortices, y-coordinates of the vortex center points and the vorticity magnitude at the vortex center are defined as follows.

$$\begin{cases} y_c = 0.4 - 0.15\sin(6\pi x_c) \\ y_c = 0.8 - 0.15\sin(6\pi x_c) \end{cases} \tag{4.8}$$

$$f = N(-1.0, 0.05^2) \tag{4.9}$$

where N means the normal distribution by which the vorticity magnitude is varied in each points. With respect to the counterclockwise vortices, y-coordinates of the vortex center points and the vorticity magnitude at the vortex center are defined as follows.

$$\begin{cases} y_c = 0.2 - 0.15\sin(6\pi x_c) \\ y_c = 0.6 - 0.15\sin(6\pi x_c) \end{cases} \tag{4.10}$$

$$f = N(1.0, 0.05^2) \tag{4.11}$$

The vorticity distribution affected by one vortex is as follows.

$$\omega_{x,y,i} = fe^{\frac{-2r_{x,y,i}}{w^2}} \tag{4.12}$$

$$r_{x,y,i} = \sqrt{(x - x_c)^2 + (y - y_c)^2} \tag{4.13}$$

$$w = N(0.3, 0.015) \tag{4.14}$$

The final vorticity distribution is obtained by sum of each vorticity as follows.

$$\omega_{x,y} = \sum_{i=1}^{n} \omega_{x,y,i} \tag{4.15}$$

The time series vorticity distributions given from the test function are shown in Fig. 19. In the case of $t = 0, 4$ leftmost vortices correspond to generated vortices at $t = 0, 4$ center vortices are that generated 100 steps before and 4 rightmost vortices are that generated 200 steps before.

In the determination of the vortex sources, the time-series vorticity matrix which contains 100 [images] × 101 [pixels] × 101 [pixels] elements is used. The threshold value is set to 0.2 for creating the BOX-STRUCTURE. The SUBBOX is created from 5 images. In the extraction of vortex trajectory, the restricted domain size is set to 20 pixels along the vertical and horizontal directions from the vortex center. The margin used to terminate the vortex extraction algorithm is set to 5 pixels for all edges for +x and ±y directions. In the reconstruction of the vortex structure, the vortex diameter used to define the effects range of the vortex is set to 30 pixels.

The reconstructed vorticities are shown in Fig. 20 and black regions correspond to the regions where the vorticity magnitude is zero. It can be confirmed that the reconstructed vorticity distributions are in good agreement with the original vorticity distributions shown in Fig. 19. At $t = 95$, the rightmost vortices disappear in the reconstructed distribution since they are considered as the out of the analysis domain based on the setting of the margin. A theoretical vortex trajectory is shown in Fig. 21. In this method, since each vortex trajectory is decomposed and extracted, the motion of each vortex can be combined into one figure. The obtained vortex trajectory is shown in Fig. 22. a.3 and a.5 respectively correspond to the vortices generated100 or 200 steps before from a.1, and then a.4 and a.6 respectively correspond to the vortices generated at 100 or 200 steps before from a.2. The relationships between b.1, b.3 and b.5 and b.2, b.4 and b.6 are the save things. In other words, there are four major vortex trajectories that are a.1, a.2, b.1 and b.2. These 4 vortex trajectories are in good agreement with the theoretical ones, so that it can be confirmed that the vortices are successfully extracted by the proposed approach.

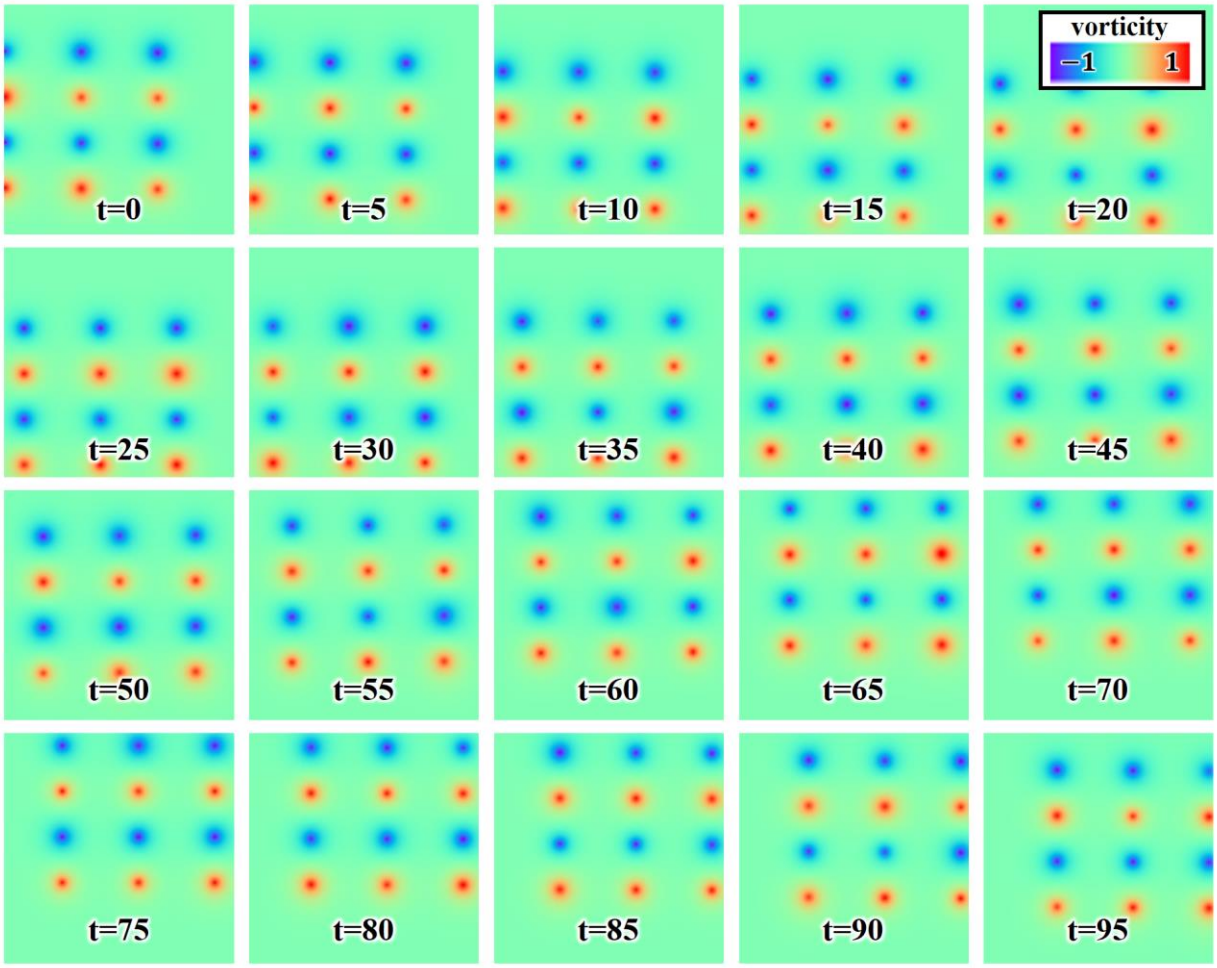

Fig. 19 Test Function for Reconstruction of Vortex Structure

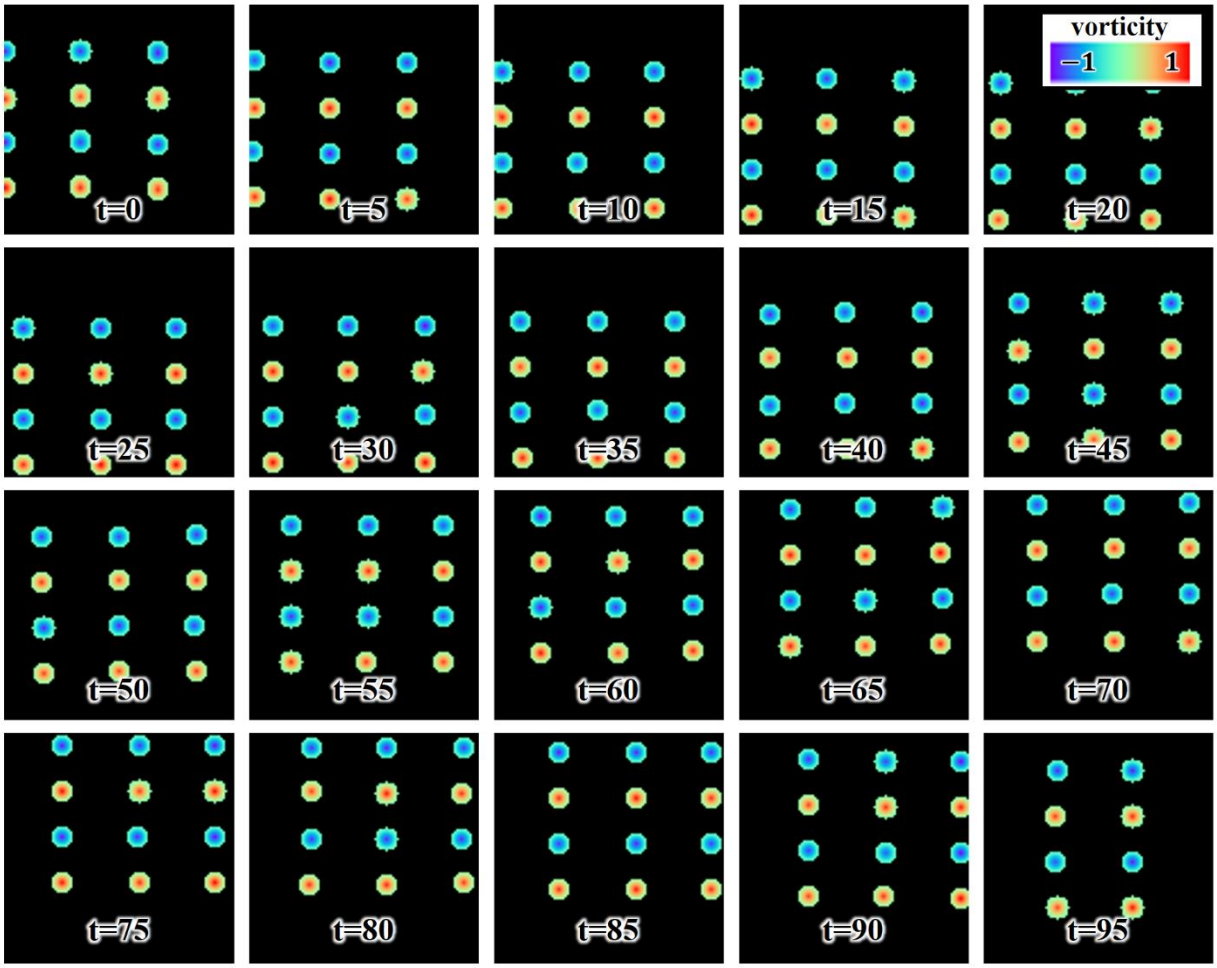

Fig. 20 Reconstructed Vortex Distribution for Test Function

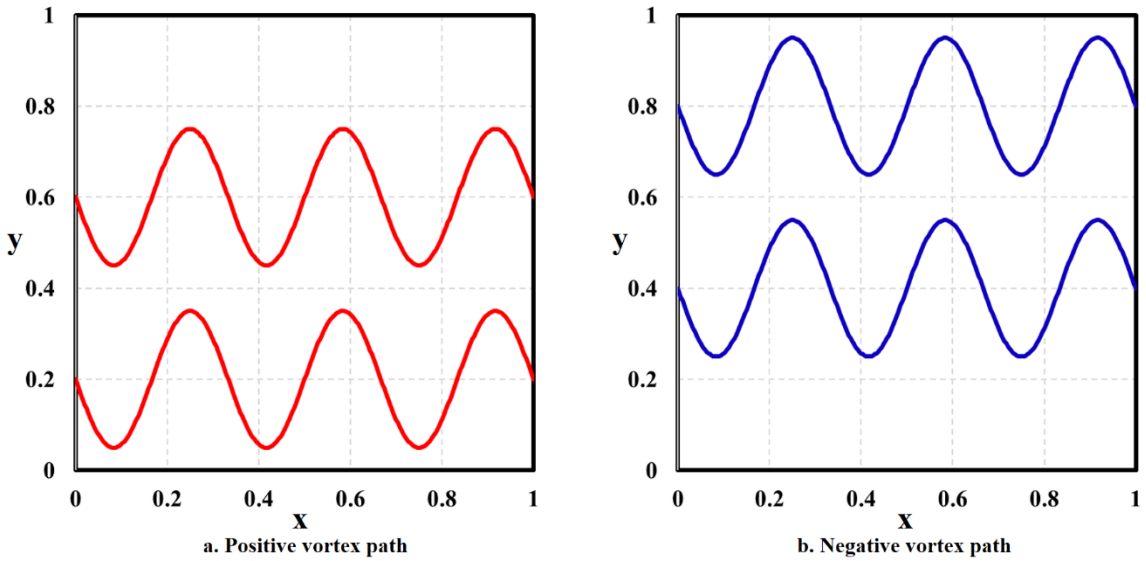

Fig. 21 Theoretical Vortex Trajectory

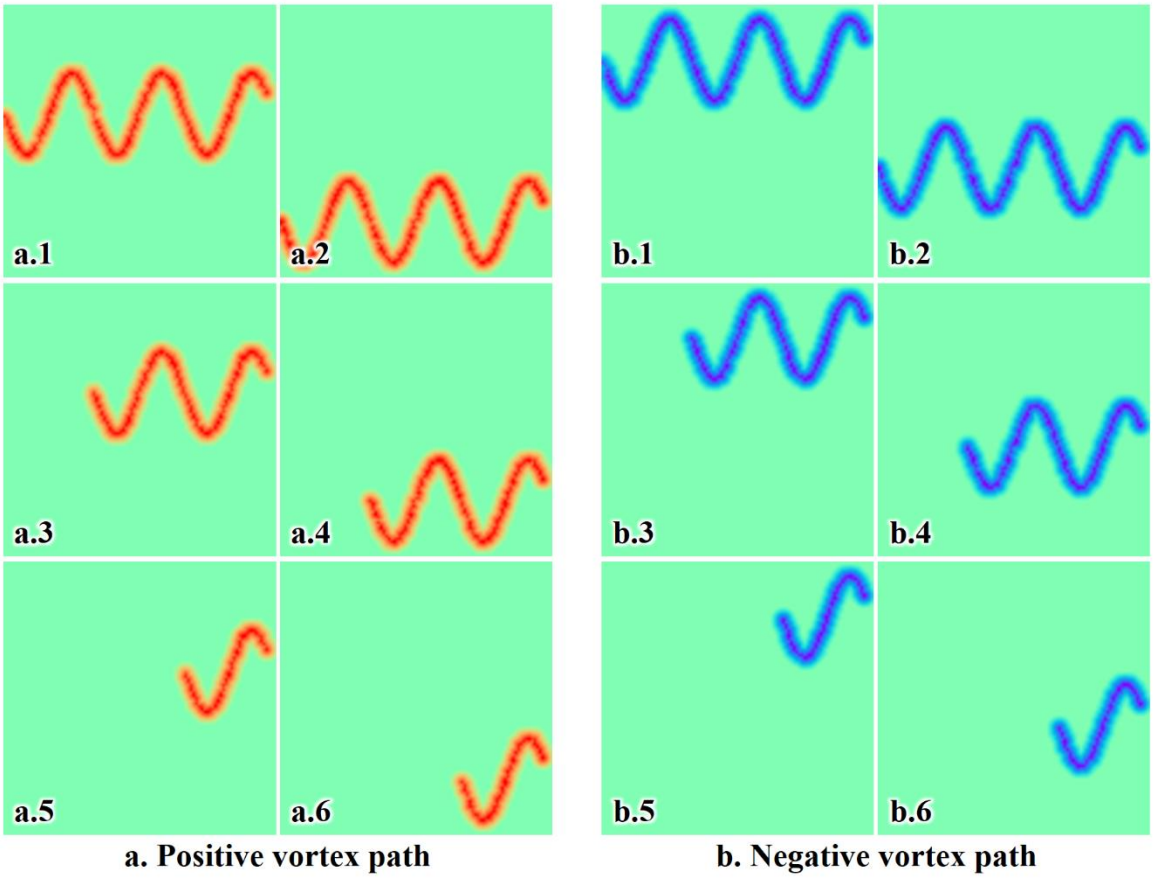

Fig. 22 Reconstructed Vortex Trajectory

F. Reconstruction of Vortex Structure around Tandem Flapping Wing Object

In order to verify the usefulness of the RVS-II, reconstruction of vortex structure is carried out for the tandem flapping wing cases of FA20-PD150 and FA40-PD90. In the determination of the vortex source, the time-series vorticity matrix which contains 80 [images] × 308 [pixels] × 299 [pixels] elements is used. The threshold value is set to 1.0 for creating the SUB-STRUCTURE. The SUBBOX is created from every 5 images. In the extraction of vortex trajectory, 15 major vortex trajectories are extracted for both of the negative and positive ones from larger elements size of SUB-STRUCTURE. The restricted domain size is set to within -20 ~ 20 pixels along the vertical direction and within -1 ~ 20 pixels along the horizontal directions from the vortex center. The margin used to terminate the vortex extraction algorithm is set to 1 pixel for all edges at $-$x direction and 10 pixels for all edges at $+$x and $\pm$y directions. In the reconstruction of the vortex structure, the vortex diameter used to define the effects range of the vortex is set to 30 pixels.

The reconstructed vortex trajectories are summarized in Figs. 23-26 and the reconstructed vortex distributions are summarized in Figs. 27-30. With respect to the reconstructed vortex trajectory for counterclockwise vortex in FA20-PD150, Fig. 23.a. indicates a vortex trajectory generated from the fore-wing at the downstroke near the top dead position. (A in Fig. 27) It is confirmed that the generated vortex (Fig. 27.a) moves backward (Fig. 27.b-c) and interrupted by the upstroke of the aft-wing (Fig. 27.d). Fig. 23.b indicates a vortex trajectory generated from the aft-wing at the downstroke near the top dead position. (B in Fig. 28) It is confirmed that the generated vortex (Fig. 28.b) moves backward (Fig. 28.c-). Fig. 23.e indicates a vortex trajectory generated from the fore-wing at the downstroke near the bottom dead position. (C in Fig. 27) It is confirmed that the generated vortex (Fig. 27.d) moves backward (Fig. 28.a-). Fig. 23.i indicates a vortex trajectory generated from the aft-wing at the downstroke near the bottom dead position. (D in Fig. 28) It is confirmed that the generated vortex (Fig. 28.d) moves backward (Fig. 27.a-). Fig. 23.j indicates a vortex trajectory generated between the fore-wing in the downstroke and the aft-wing in the upstroke. This

vortex trajectory is considered as the same one observed in Fig. 14. (E in Fig. 27) It is confirmed that the generated vortex (Fig. 27. c) moves backward (Fig. 27.d) and then the vortex follows the upstroke of the aft-wing (Fig. 28.a). With respect to the reconstructed vortex trajectory for clockwise vortex in FA20-PD150, Fig. 24.a indicates a vortex trajectory generated from the fore-wing at the downstroke. (F in Fig. 27) It is confirmed that the generated vortex (Fig. 27.c) follows the upstroke of the aft-wing (Fig. 27.d and Fig. 28.a), and the vorticity of the vortex becomes larger by the downstroke of the aft-wing (Fig. 28.b-c), and then the vortex moves backward (Fig. 28.d and Fig. 27.a-). Fig. 24.i indicates a vortex trajectory generated from the fore-wing at the downstroke near the bottom dead point. (G in Fig. 28) It is confirmed that the generated vortex (Fig. 28.a, it is not clearly confirmed due to sparse smoke distribution) moves backward (Fig. 28.c), and the vortex becomes stronger by the downstroke of the aft-wing (Fig. 28.d), and then the vortex moves backward (Fig. 27.a-). With respect to the reconstructed vortex trajectories and the reconstructed vortex distributions in FA40-PD90, it can also be confirmed that major vortex structures are efficiently extracted. Although additional more detailed discussion will be required, it can be concluded from the present results that the proposed RVS-II approach can extract vortex structures in a much better way than RVS-I, and then the proposed approach can facilitate the physical understanding of complex vortical flowfield.

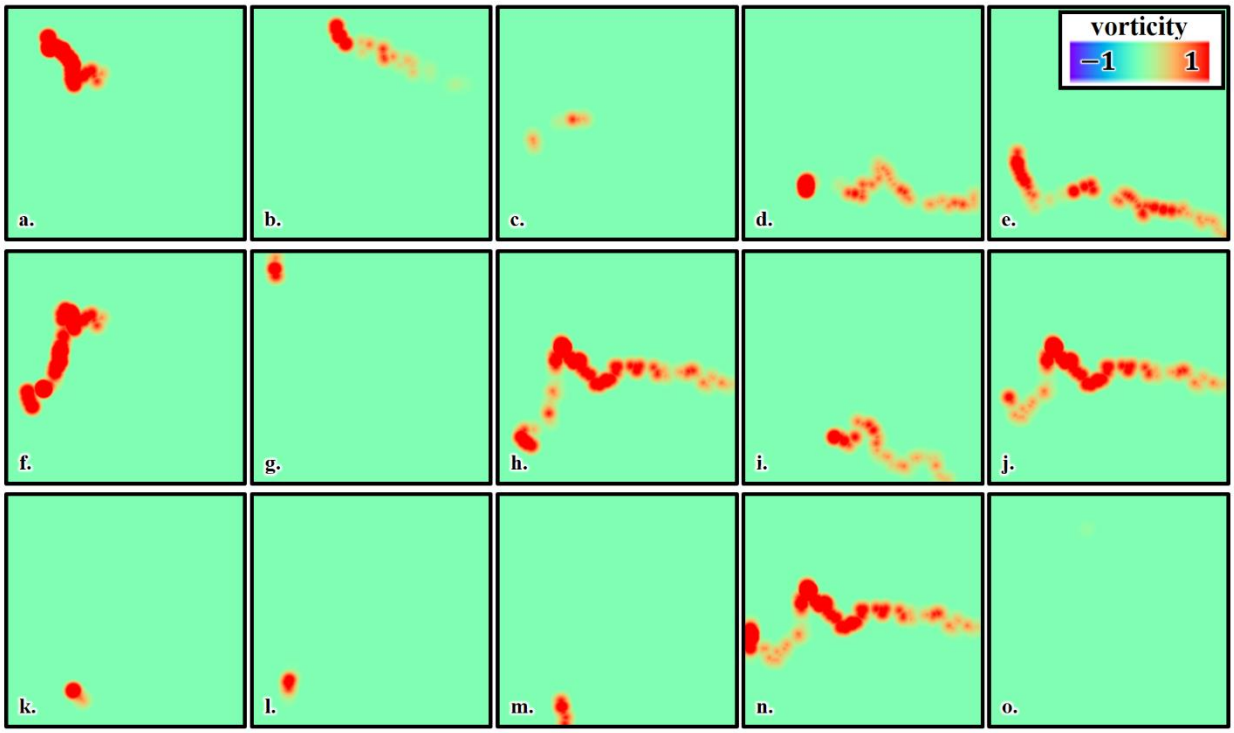

Fig. 23 Reconstructed Vortex Trajectory for Counterclockwise Vortex in FA20-PD150

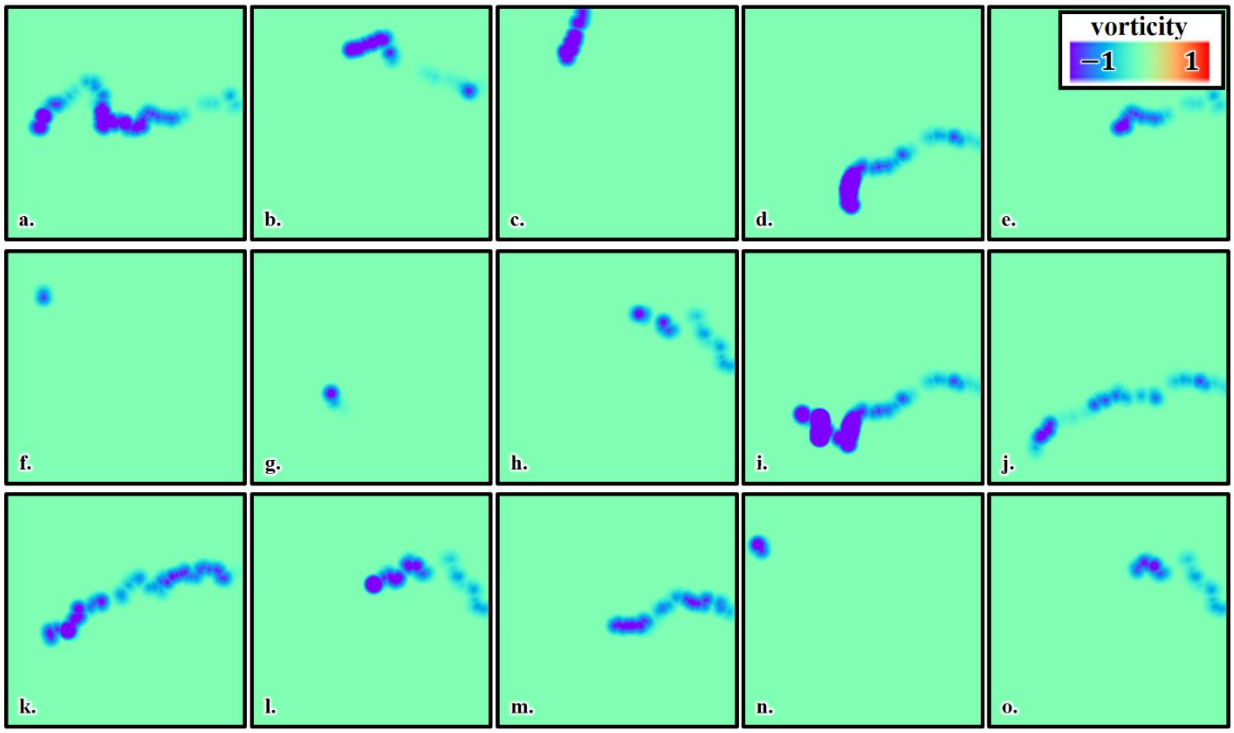

Fig. 24 Reconstructed Vortex Trajectory for Clockwise Vortex in FA20-PD150

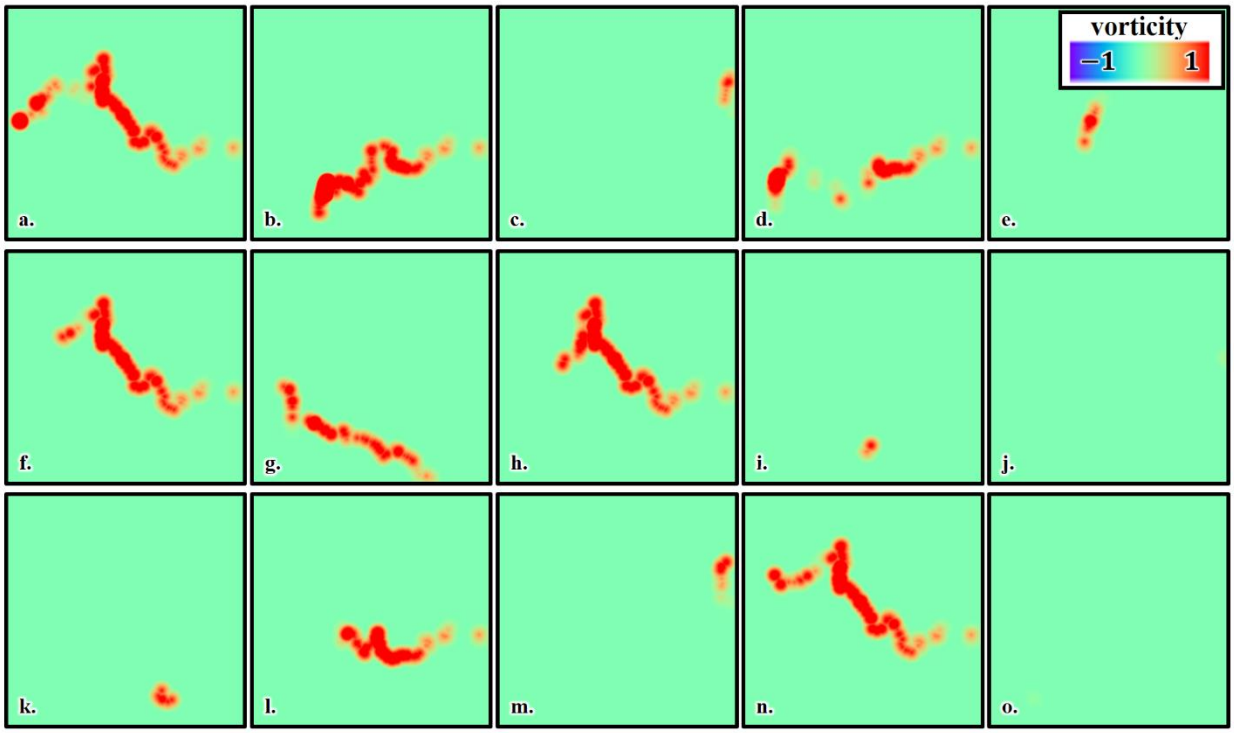

Fig. 25 Reconstructed Vortex Trajectory for Counterclockwise Vortex in FA40-PD90

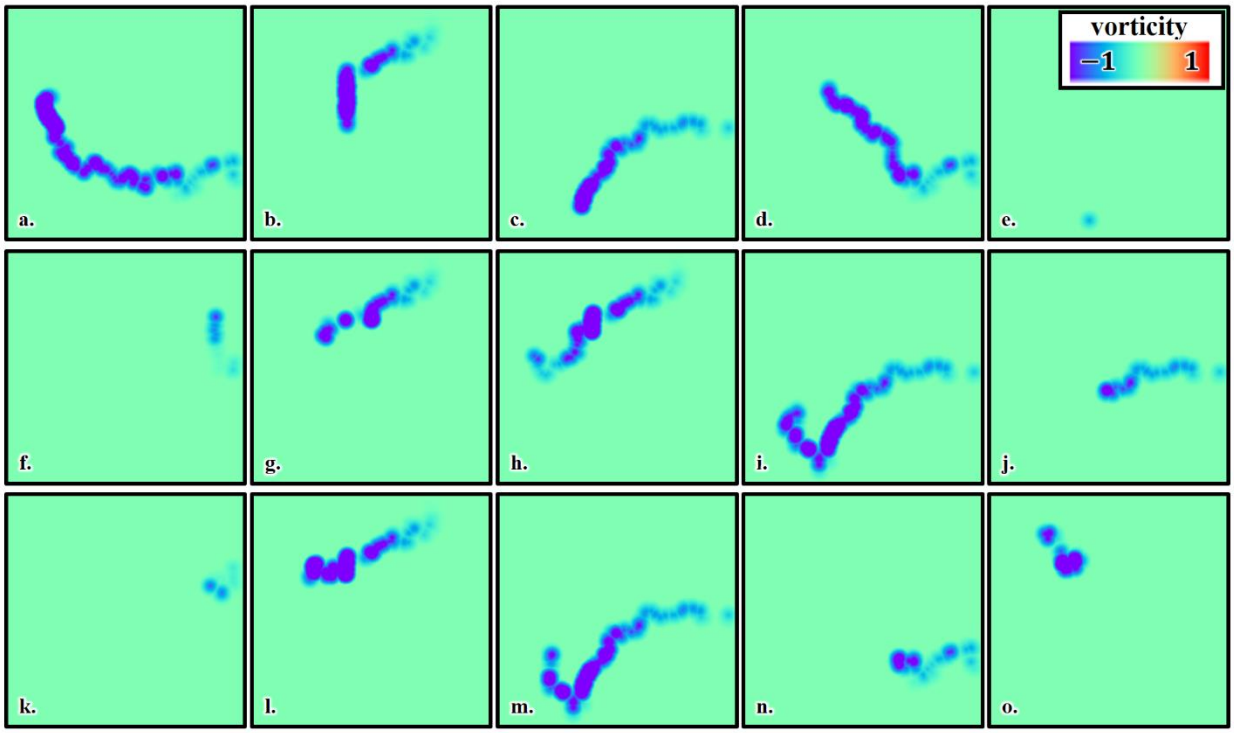

Fig. 26 Reconstructed Vortex Trajectory for Clockwise Vortex in FA40-PD90

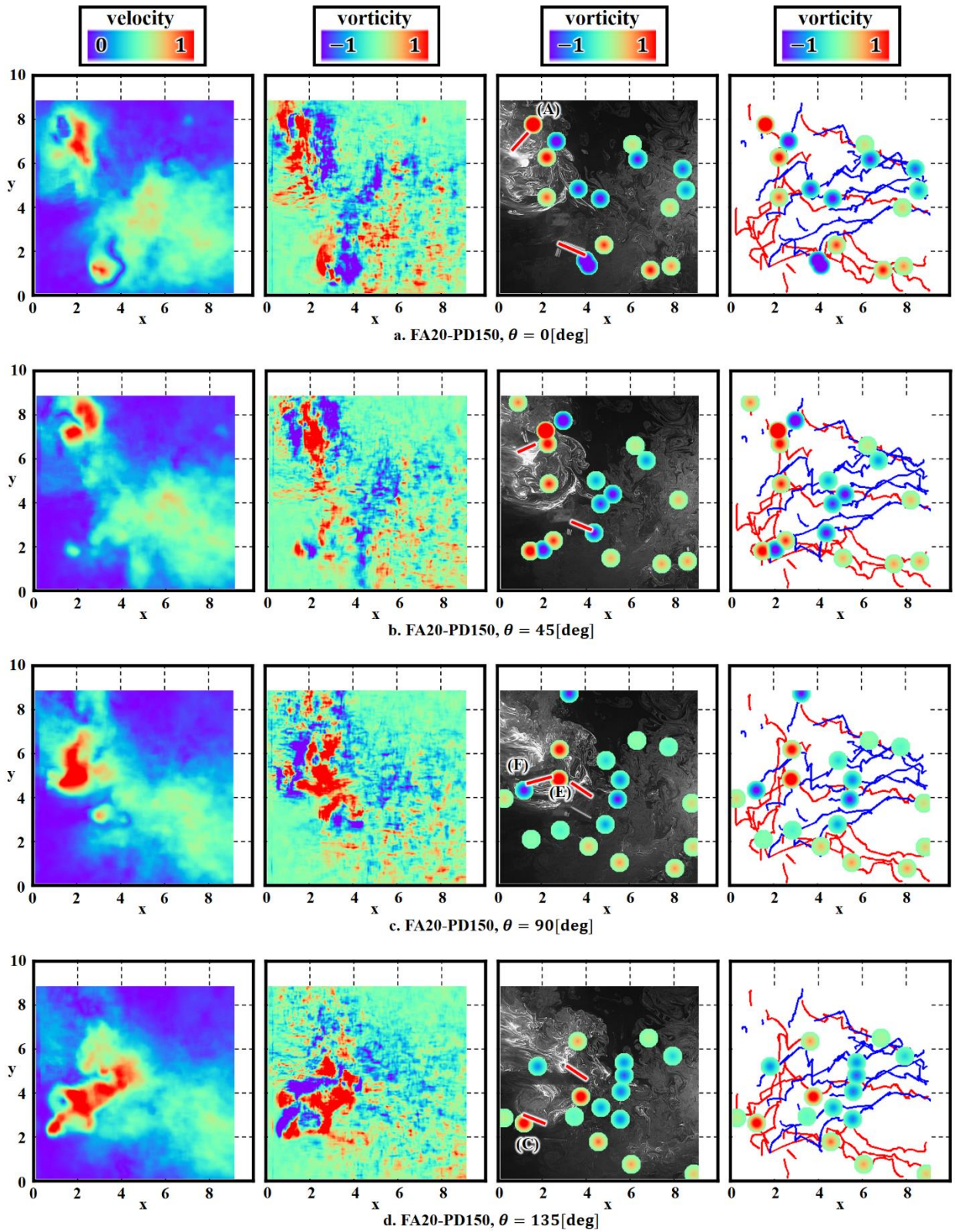

Fig. 27 Reconstructed Vortex Distribution in FA20-PD150 at Downstroke of Fore-wing

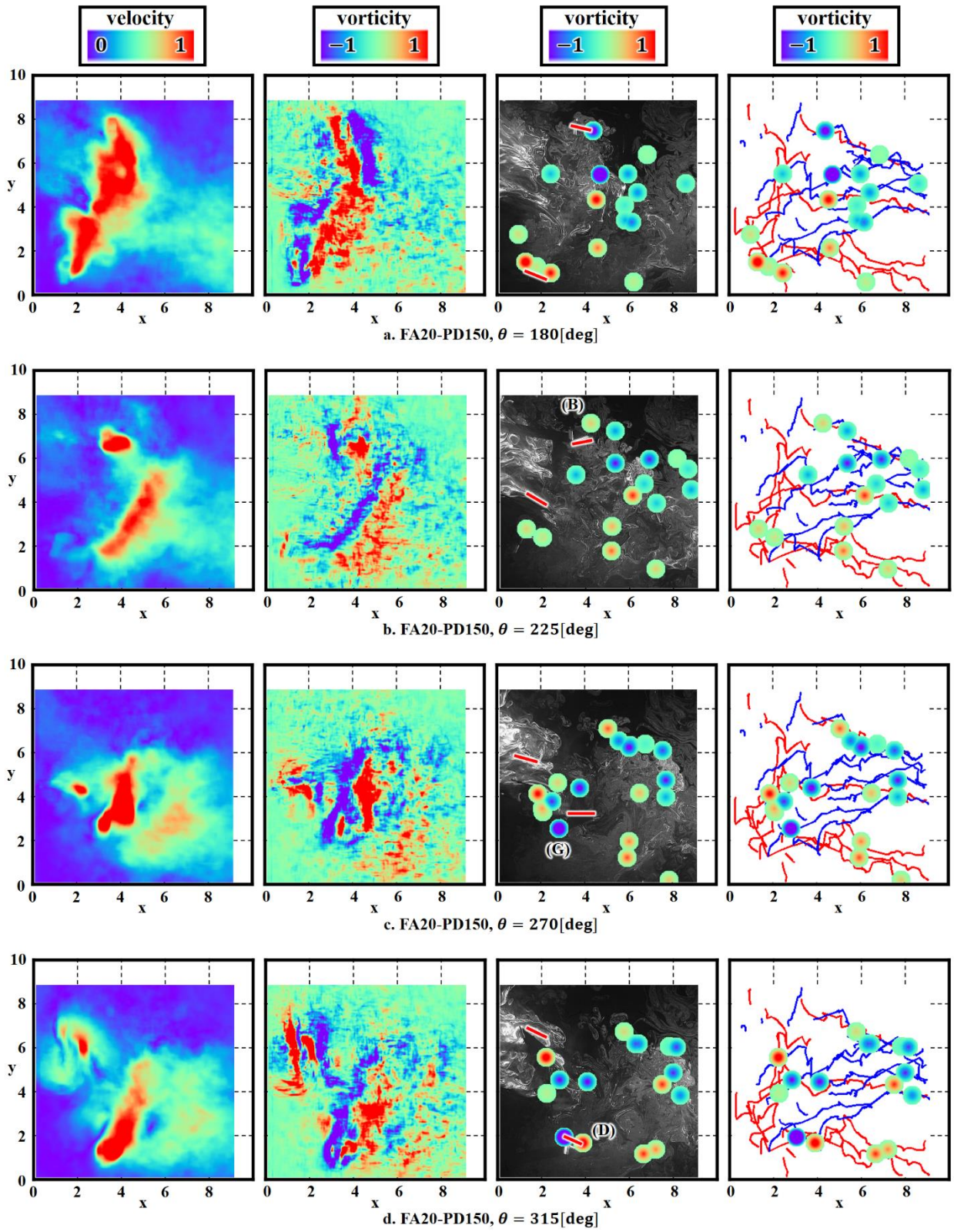

a. FA20-PD150, $\theta = 180$[deg]

b. FA20-PD150, $\theta = 225$[deg]

c. FA20-PD150, $\theta = 270$[deg]

d. FA20-PD150, $\theta = 315$[deg]

Fig. 28 Reconstructed Vortex Distribution in FA20-PD150 at Upstroke of Fore-wing

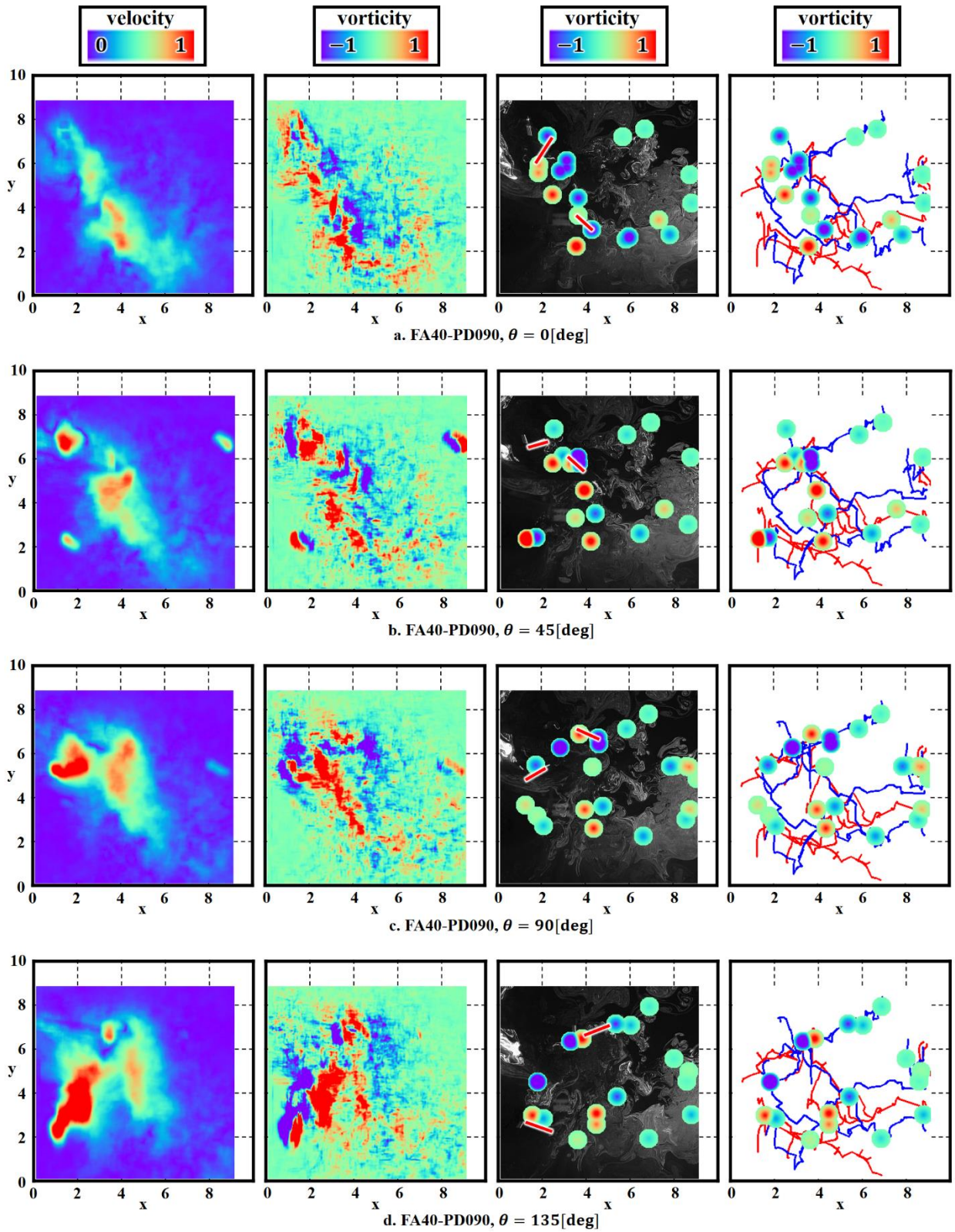

Fig. 29 Reconstructed Vortex Distribution in FA40-PD90 at Downstroke of Fore-wing

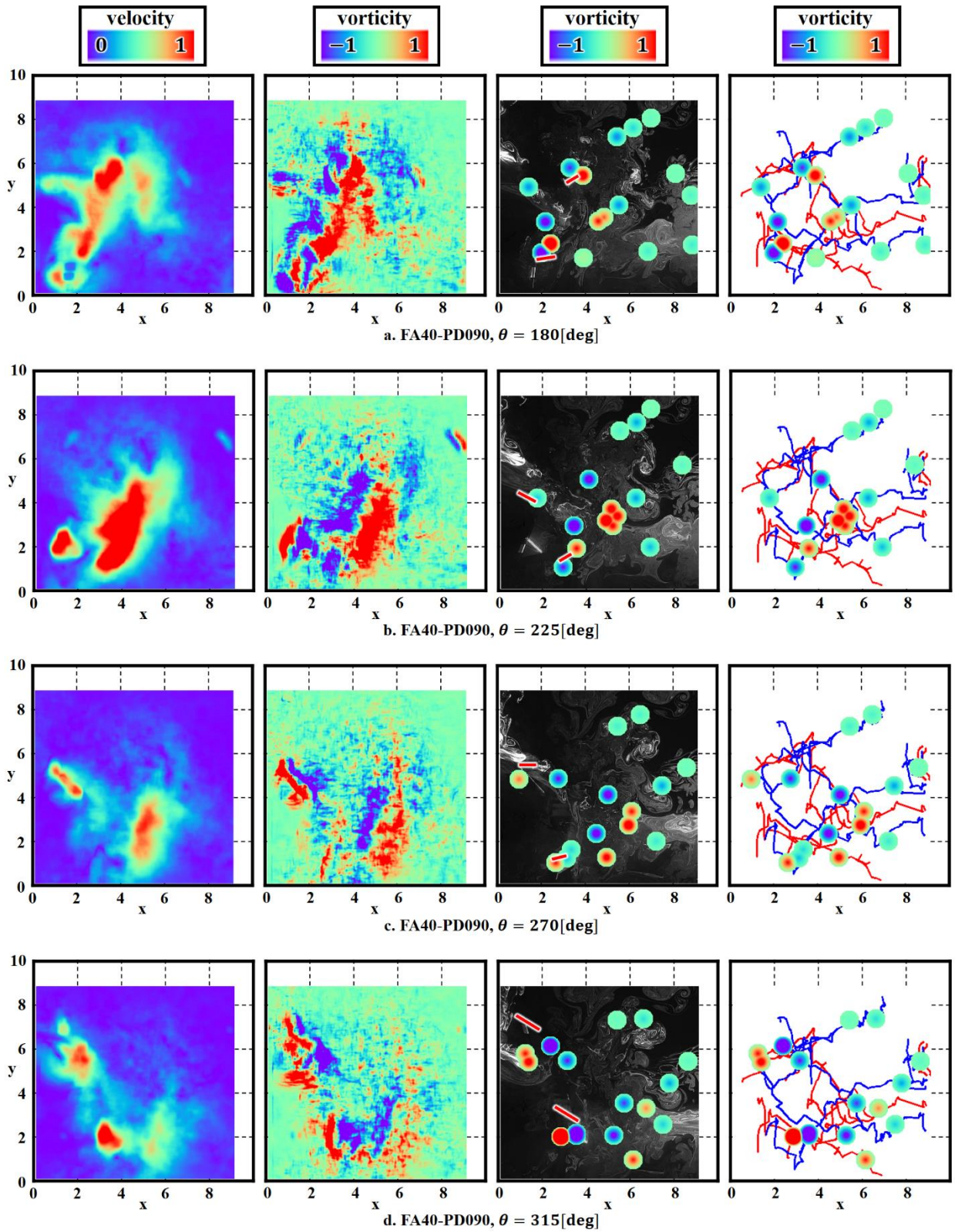

Fig. 30 Reconstructed Vortex Distribution in FA40-PD90 at Upstroke of Fore-wing

V. Conclusions

In this research, we developed a reconstruction method of major vorticity distribution as postprocessing method of PIV analysis with the purpose of assisting physical understanding of vorticity distribution for tandem flapping wing object mimicked dragonfly. With respect to the self-developed flapping wing object, its flapping angle, phase difference between the fore / aft wings and feathering angle can be adjusted. In this research, the developed reconstruction method is applied to two characteristic conditions. First case is ± 20 [deg] of the feathering angle, 150 [deg] of the phase difference and ±45 [deg] of the flapping angle. The other case is ± 40 [deg] of the feathering angle, 90 [deg] of the phase difference and ±45 [deg] of the flapping angle. In the PIV measurement, a high speed camera was used to take sequential images in the enclosed region with oil mist as tracer particles and Nd: YAG laser as a light source. The Reynolds number is 2741 with the reference length of the chord length of the single wing and the reference velocity of the wing tip flapping velocity. The flapping frequency was roughly 2.35 Hz to 3.12 Hz.

In the reconstruction method for the major vorticity distribution I (RVS-I), an optical flow method with Farneback method was used for PIV analysis. The velocity distributions obtained by the PIV analysis is ensemble averaged to treat the data loss in the flowfield. Vorticity distributions in spatial two-dimension (x, y) and temporal one-dimension (t) are compiled into (x, y, t) three-dimensional space. Then the visualization area is restricted by setting an appropriate threshold value. And then, an ideal path as a vortex trajectory is extracted from the restricted visualized region by using RVS-BCC method and RVS-GSS method. The vortex trajectory is optimized by using Brute Force method and Brent method. The extracted vortex trajectory is removed from the original vortex distribution, and an ideal path as a vortex trajectory is extracted from the remaining vortex distribution once again. Multiple paths of dominant vortices are extracted by repeating this extraction process. Finally, the reconstruction of the major vortex distribution is executed by using the information of the vortex trajectories and the strength of the vortices. The developed method could clearly reconstruct small vortex structures in the backward of the flapping wing object which was difficult to discriminate from the original vorticity distributions.

In the reconstruction method for the major vorticity distribution II (RVS-II), the algorithm was developed to improve the RVS-I algorithm for lower-cost and higher-accuracy. The RVS-II algorithm can drastically reduce the computational cost by decomposing the input time-series data and iteratively extracting the local vortex trajectory for each decomposed data, and it could also improve the extraction accuracy by decomposing the input time-series data and setting a threshold for each decomposed data. The RVS-II method could extract major vortex structures in a much better way than RVS-I, and then it was confirmed that the proposed approach could facilitate the physical understanding of complex vorticial flowfield.

In the present algorithm, there are many parameters users have to specify. A threshold value and a division number have to be set to detect vortex sources. A vortex trajectory number, restricted domain size, and analysis domain have to be set to extract vortex trajectories. A vortex diameter have to be set to reconstruct the vortex structure. The developed algorithm of the RVS-II has to be expanded to reduce the number of parameters users have to specify in our future works.

Acknowledgments

The authors would like to thank Mr. Hirofumi Tsuchida for technical assistance for the PIV measurements.

References

[1] Shyy, W., Lian, Y., Tang, J., Viieru, D., and Liu, H., "Aerodynamics of Low Reynolds Number Flyers," Cambridge Univ. Press, New York, 2008.

[2] M. A., Groen, "PIV and Force Measurements on the Flapping-wing MAV DelFly II," Master of Science Thesis, December 20, 2010.

[3] Jones, M., and Yamaleev, N., "Adjoint-based Shape and Kinematics Optimization of Flapping Wing Propulsive Efficiency," AIAA 2013-2472, 2013.

[4] Broering, M., T., Yongsheng, L., "The Effect of Spacing on Tandem Wing Aerodynamics," 28th AIAA Computational Fluid Dynamics Conference, 2010.

[5] Richter, C., Lipson, H., "Untethered Hovering Flapping Flight of a 3D-Printed Mechanical Insect," 12th International Conference on Artificial Life , pp.787-803, 2010.

[6] Fuchiwaki, M., Kuroki, T., Tanaka, K., Tabata, T., "Wake Structure Behind a Free Flight Butterfly and its Growth Process," 16th International Symposium on Flow Visualization, 2014.

[7] Jones, R., Cleaver, J., D., Gursul, I., "Fluid-Structure Interactions for Flexible and Rigid Tandem-Wing at Low Reynolds Numbers," 53rd AIAA Computational Fluid Dynamics Conference, 2015.

[8] Yamazaki, W., Akimoto, R., and Yamada, H., "PIV Data Reconstruction via Proper Orthogonal Decomposition with a Cross Validation Approach," Journal of Fluid Science and Technology 9:4, JFST0066-JFST0066, 2014.

[9] Tsuchida, H., and Yamazaki, W., "Aerodynamic Characterictics and PIV Measurement around Tandem Flapping Wings," Fourteenth International Conference on Flow Dynamics, 2016.

[10] Johnr, F., and Johnk, E., "Turbulence modification by particles in a backward-facing step flow" Journal of Fluid Mechanics, vol. 394, pp. 97–117, 1999.

[11] B. K. P., Horn, and B., Schunk, "Determining Optical Flow," Artificial Intelligence, vol. 17, pp. 185-203, 1981

[12] Farnebäck, G., "Two-frame Motion Estimation Based on Polynomial Expansion," In Proceedings of the Scandinavian conference on image analysis, 2003.

[13] T. C., Lee, R. L., Kashyap, and C. N., Chu, "Building skeleton models via 3-D medial surface/axis thinning algorithms," Computer Vision, Graphics, and Image Processing, 56(6):462-478, 1994.

[14] Kurlin, V. "A one‐dimensional homologically persistent skeleton of an unstructured point cloud in any metric space." Computer Graphics Forum. Vol. 34. No. 5. 2015.

[15] Kurlin, V. "Auto-completion of Contours in Sketches, Maps, and Sparse 2D Images Based on Topological Persistence." Symbolic and Numeric Algorithms for Scientific Computing (SYNASC), 2014.

[16] Chernov, A. and Kurlin, V. "Reconstructing persistent graph structures from noisy images." Image-a, vol 3(5) p.19-22, 2013.

[17] Press, W. H., Teukolsky, S. A., Vetterling, W. T, and Flannery, B. P., "Numerical Recipes in C," The Art of Scientific Computing, 2nd Ed., University of Cambridge Press, Cambridge, United Kingdom, 1992.

[18] J., More, "The Levenberg-Marquardt Algorithm Implementation and Theory," Numerical Analysis, G.A. Watson, ed., Springer-Verlag, 1977.